LA-14043-MS
Issued: June 2003

Geology of the North-central to Northeastern Portion of Los Alamos National Laboratory, New Mexico

Alexis Lavine
Claudia J. Lewis
Danielle K. Katcher
Jamie N. Gardner
Jennifer Wilson*

* Earth & Environmental Science Department, New Mexico Institute of Mining & Technology, 801 Leroy Place, Socorro, NM 87801, jenw@nmt.edu

Los Alamos
NATIONAL LABORATORY

Contents

Abstract 1

I. Introduction 2

II. Previous Work 4

III. Methods 7
- A. Geologic Mapping 7
- B. Structural Analysis 8
- C. Mineralogy, Petrography, and Geochemistry 8
- D. Notes on Units of Measure 9

IV. Geology 10
- A. Stratigraphy 10
  - A.1 Otowi Member of the Bandelier Tuff (Qbo) 10
  - A.2 Cerro Toledo interval (Qct) 10
  - A.3 Tshirege Member of the Bandelier Tuff (Qbt) 10
  - A.4 Older Alluvial Deposits (Qoal) 14
  - A.5 Recent Alluvial and Terrace Deposits (Qal+Qt) 14
  - A.6 Colluvium (Qc) 14
  - A.7 Artificial Fill 14
- B. Mineralogy and Geochemistry of Tshirege Member Units 14
  - B.1 Mineralogy 14
  - B.2 Geochemistry of Tshirege Member Units 16
- C. Structural Geology 17
  - C.1 Faults 17
  - C.2 Zones of Changes in Dip of Stratigraphic Markers 22

V. Discussion 22
- A. Stratigraphy of Tshirege Member and Post-Bandelier Tuff Units 22
  - A.1 Comparison of Tshirege Member Units to Previous Studies 22
  - A.2 Post-Bandelier Tuff Units 27
- B. Structural Geology 27
- C. Implications for Contaminant Transport 29
- D. Potential for Seismic Surface Rupture and Age of Faulting 29

VI. Conclusions 30

VII. Acknowledgements 30

References 31

Appendix A. Maps Showing Sample Locations for Stratigraphic Sections 37

Appendix B. Minerology of Samples from Whole-Rock X-Ray Diffraction Analyses 41

Appendix C. Whole-Rock Geochemistry 43

List of Figures

Figure 1. Map of the Rio Grande rift in northern New Mexico. 2

Figure 2. Map of the Pajarito fault system in the vicinity of Los Alamos National Laboratory. 3

Figure 3. Generalized stratigraphy of lower units of the Bandelier Tuff and Cerro Toledo interval exposed in the study area. 5

Figure 4. Comparison of stratigraphic nomenclature of the lower portion of the Tshirege Member of the Bandelier Tuff. 6

Figure 5. Photograph of the Tshirege Member of the Bandelier Tuff in the southeast portion of the study area 12

Figure 6. Photograph of the Tshirege Member of the Bandelier Tuff in the northwestern part of the study area. 12

Figure 7. Variation diagrams showing mineralogy of tuffs in stratigraphic sections AHF-S-1, AHF-S-2, AHF-M-1, and AHF-M-2 in relation to elevation and mapped subunits within the Tshirege Member. 15

Figure 8. Major element oxide variation diagrams. 16

Figure 9a. Outcrop photograph of fault F1. 18

Figure 9b. Schematic diagram showing the structural elements of fault F1. 18

Figure 9c. Back-scattered electron (BSE) microprobe image of a deformation band from fault F1. 18

Figure 10a. Back-scattered electron image of the slip surface of fault F1. 19

Figure 10b. X-ray image of Fe- and Sn-oxide mineralization on the open slip surface of fault F1. 19

Figure 11a. Photograph of fracture or fracture-based fault in fault zone F2. 19

Figure 11b. Photograph of possible deformation band fault in fault zone F2. 20

Figure 11c. Photograph of fracture-based fault in fault zone F2. 20

Figure 12. Rose diagram of strikes of fracture data from fault and fracture zone F2. 21

Figure 13a. Contoured upper surface of unit Qbt1g. 23

Figure 13b. Contoured upper surface of unit Qbt1v-c. 24

Figure 13c. Contoured upper surface of unit Qbt1v-u. 25

Figure 13d. Contoured upper surface of unit Qbt2. 26

Figure A-1. Geologic map showing the location of samples from stratigraphic section AHF-S-1. 37

Figure A-2. Geologic map showing the location of samples from stratigraphic section AHF-S-2. 38

Figure A-3. Geologic map showing the location of samples from stratigraphic section AHF-M-1. 39

Figure A-4. Geologic map showing the location of samples from stratigraphic section AHF-M-2. 40

Plate 1. Geologic map of the north-central to northeastern part of Los Alamos National Laboratory (inside rear cover)

Plate 2. Cross Sections A-A' and B-B' (inside rear cover)

Plate 3. Lithologic descriptions of stratigraphic sections of the Tshirege Member of the Bandelier Tuff in Sandia and Mortandad canyons (inside rear cover)

Geology of the North-central to Northeastern Portion of Los Alamos National Laboratory, New Mexico

Alexis Lavine, Claudia J. Lewis, Danielle K. Katcher, Jamie N. Gardner, and Jennifer Wilson

ABSTRACT

Geologic mapping and related field and laboratory investigations to assess seismic hazards in the north-central to northeastern portion of Los Alamos National Laboratory (LANL) revealed only small faults that have little potential for seismic surface rupture. These faults likely represent subsidiary ruptures associated with hanging wall deformation within the Pajarito fault system. The 7.5 km^2 study area lies ~1 km east of mapped faults of the Pajarito fault system, ~2.5 km south of the southernmost mapped trace of the Sawyer Canyon fault, and within a zone of inferred, subsurface, pre-Bandelier Tuff faults. Mapped changes in welding and crystallization in the Tshirege Member of the Bandelier Tuff coincide with or parallel stratigraphic contacts, providing large-scale, mostly planar markers that are useful for evaluating structural offset. Lateral variations in welding in units Qbt1v and Qbt2 have led us to modify stratigraphic nomenclature for this part of the Tshirege Member. Field studies and analysis of map data in 2-D and 3-D identified the following fault and fracture zones: (1) a 15–20-cm-wide fault with an unknown amount of displacement, exposed in unit Qbt3 near building 53-3f, that is oriented N16E, 82SE and consists of densely spaced deformation bands; (2) an ~180-m-wide zone of abundant fractures and faults that range in width from 1–60 cm, have a mean strike of N12E ± 26° and a mean dip of 87 ± 5º, are exposed in unit Qbt3 north of the lagoons at TA-53, and have an unknown amount of displacement; (3) a 60-m-wide fault zone, exposed in units Qbt1g through Qbt2 in a small tributary canyon to Sandia Canyon, with ~1.2 m of down-to-the-northwest displacement on units Qbt1g through Qbt2; and 4) three small (<1.5 m of vertical separation on Tshirege Member units) faults in the western portion of the map area. Three-dimensional structural analysis reveals changes in dip of mapped contacts that coincide with faults, suggesting that some of the faults and fracture zones may be related to distributed deformation above deep-seated faults. However, changes in dip of Tshirege Member units become less pronounced up section, suggesting that, alternatively, they likely result from deposition over paleotopography.

I. Introduction

LANL is located on the Pajarito Plateau, which is bounded on the west by the Pajarito fault system and on the east by White Rock Canyon of the Rio Grande. The Pajarito Plateau is formed primarily of the Bandelier Tuff, which was erupted at 1.6 and 1.2 Ma (Izett and Obradovich, 1994) from the Toledo and Valles calderas as a series of pyroclastic flows (e.g., Bailey et al., 1969; Gardner et al., 1986). In the area of LANL, the Pajarito fault system is the active western boundary of the Rio Grande rift, an area of predominantly east-west extension that runs from Colorado to Mexico (Figure 1). The Rio Grande rift is an active tectonic and magmatic province (e.g., Kelley, 1979; Manley, 1979; Sanford et al., 1991; Baldridge et al., 1995; Kelson and Olig, 1995; Wolff and Gardner, 1995; Machette et al., 1998; Steck et al., 1998), and has been active for at least 30 million years (e.g., Riecker, 1979; Baldridge et al., 1984; Keller, 1986). Because the western portion of LANL lies in the Pajarito fault system, many recent studies by the LANL Seismic Hazards Program have focused on surface rupture hazards to individual facilities and proposed building sites (Wong et al., 1991; Kolbe et al., 1994, 1995; Gardner et al., 1998, 1999, 2001; Olig et al., 1998; Reneau et al., 1995, 2002).

Additionally, paleoseismicity and ground motion hazards for the local area have been studied in and around Los Alamos (e.g., Wong et al., 1995, 1996; Olig et al., 1996; McCalpin, 1998, 1999; Gardner et al., in prep.). The Pajarito fault system includes the Pajarito, Rendija Canyon, and Guaje Mountain faults (Figure 2). Along the western portion of LANL, the Pajarito fault system ranges from approximately 3 to 6 km (2–4 miles) wide, and is expressed as a complex series of faults and folds (Figure 2). In the northern portion of LANL, west of the study area, the Pajarito fault system is at least 6 km (4 miles) wide (Gardner et al., 1998, 1999; Lewis et al., unpublished mapping). In addition to the Pajarito fault system, the Sawyer Canyon fault and Puye fault to the north and northeast of LANL, respectively, are dominantly down-east faults associated with the western margin of the Rio Grande rift in the area of Los Alamos (Carter and Gardner, 1995).

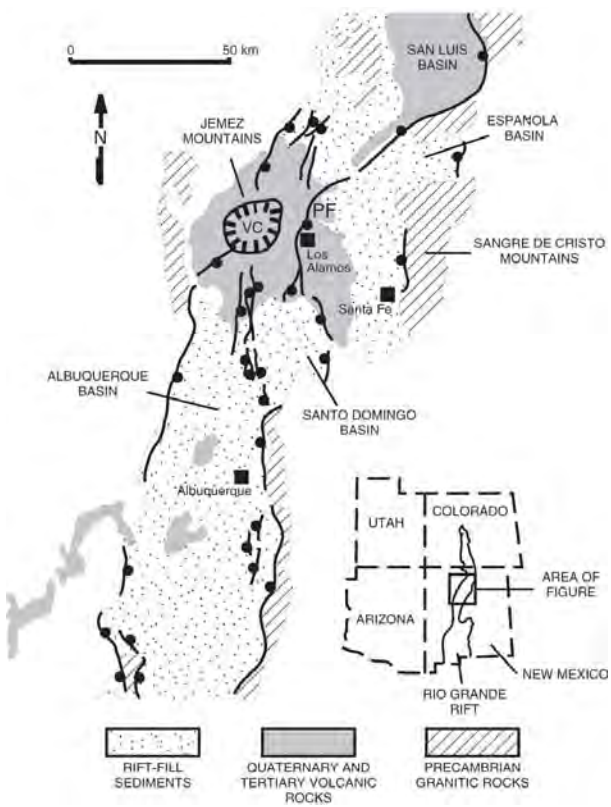

Figure 1. Map of the Rio Grande rift in northern New Mexico. Major fault systems are shown schematically (ball on downthrown side). Abbreviations: PF, Pajarito fault; VC, Valles-Toledo caldera complex, the source of the Bandelier Tuff. (modified from Gardner and Goff, 1984)

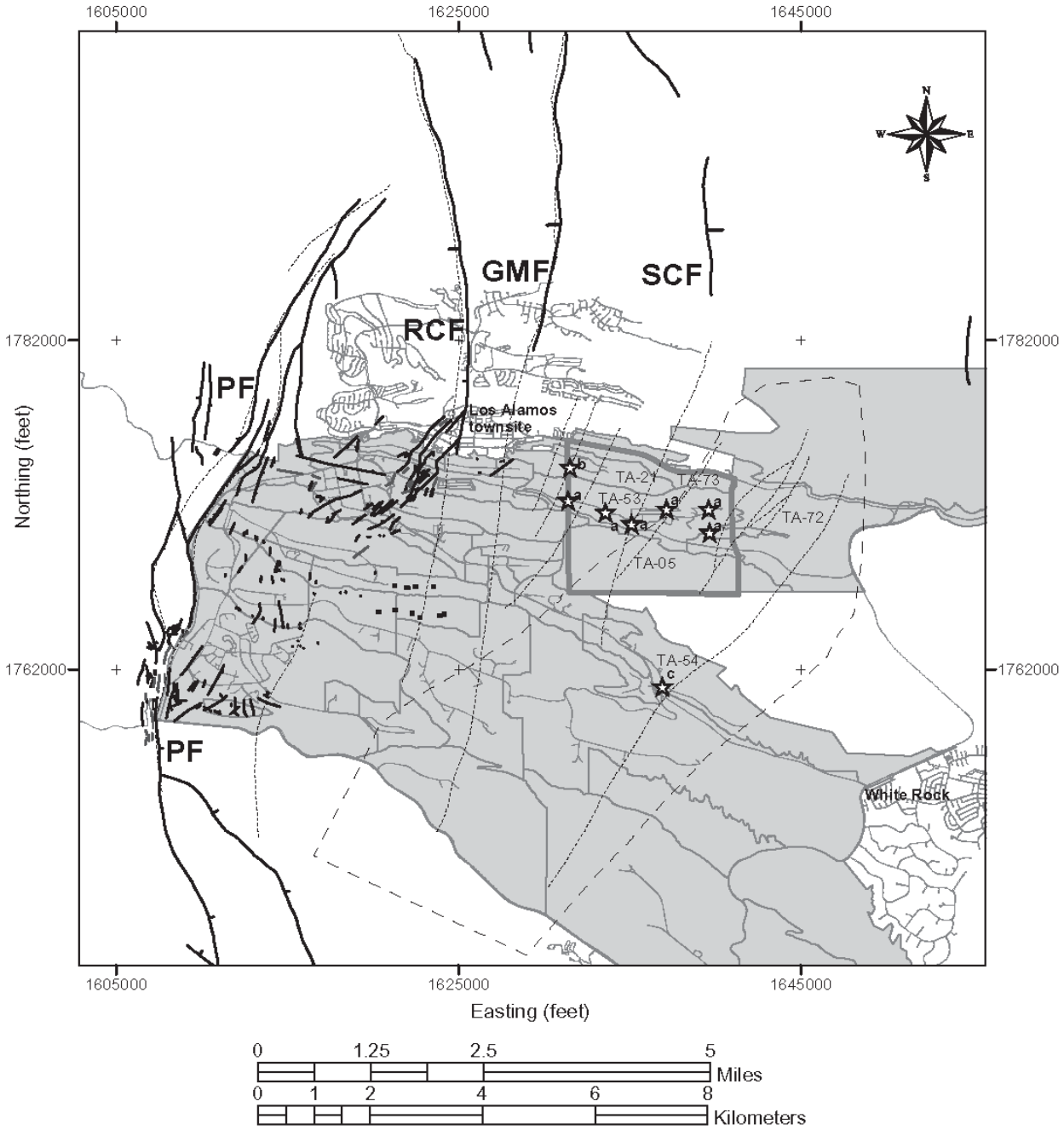

Figure 2. Map showing the Pajarito fault system in the vicinity of Los Alamos National Laboratory (shaded gray area shows the extent of LANL at time of study) and the study area for this project (thick gray outline). Faults and related folds shown in black are from Gardner and House (1987), Reneau et al. (1995), Gardner et al. (1999, 2001), Lewis et al. (2002), and Gardner and Reneau (unpublished mapping). Dashed lines are inferred subsurface faults from Dransfield and Gardner (1985). White stars mark the locations of faults or fracture zones as follows: a, this study; b, Wohletz (1995); and c, Reneau et al. (1998a). Small-displacement faults were found up to 1.6 km east of the star marked "c." The area inside the dashed black outline is the approximate location of a pre-Bandelier Tuff trough inferred from borehole and geophysical data by Broxton and Reneau (1996). Abbreviations: PF, Pajarito fault; RCF, Rendija Canyon fault; GMF, Guaje Mountain fault; SCF, Sawyer Canyon fault.

Paleoseismic investigations indicate that magnitude 6 to 7 earthquakes have occurred on the Pajarito fault system, and there is evidence for at least two large seismic events in the Holocene (Gardner et al., 1990; Wong et al., 1995; Kelson et al., 1996; McCalpin, 1998, 1999; Reneau et al., 2002; Gardner et al., in prep.), one possibly as recently as about 2 ka (McCalpin, 1998). Because earthquakes of magnitude 6 or greater commonly can cause surface rupture, surface rupture hazards should be assessed for all hazardous facilities at LANL. Although no earthquakes of this magnitude have occurred on the Pajarito fault system historically, some recent small earthquakes (M<2) within the Pajarito fault system have caused widespread effects, felt with Modified Mercalli Intensities up to VI (Gardner and House, 1994, 1999).

This report describes the results of geologic mapping and related investigations performed in the north-central to northeastern portion of LANL to assess the potential for seismic surface rupture that could affect future facilities. The area mapped is located within Technical Areas (TAs) 53, 5, 21, 72, and 73, and spans Los Alamos, DP, Sandia, and Mortandad canyons, DP Mesa, Mesita de Los Alamos, and a narrow mesa between Sandia and Mortandad canyons (Figure 2, Plate 1). Surface ruptures associated with the Pajarito fault system have been mapped in detail to approximately 1 km (0.6 miles) west of the study area (Figure 2; Gardner et al., 1999). The southern extent of the Sawyer Canyon fault has been mapped to approximately 2.5 km (1.5 miles) north of the study area (Carter and Gardner, 1995), and a zone of horsts and grabens has been mapped approximately 1.5 km (~1 mile) south of the study area (Reneau et al., 1998a).

The most widespread and oldest stratigraphic unit exposed in the study area is the early Pleistocene Bandelier Tuff. Geologic units exposed at the surface in the study area include the Otowi Member of the Bandelier Tuff, the Cerro Toledo interval, units Qbt1 through Qbt3 of the Tshirege Member of the Bandelier Tuff (Figure 3), and post-Bandelier Tuff alluvial and colluvial deposits. The primary unit exposed within the study area is the 1.2-million-year-old Tshirege Member of the Bandelier Tuff, which comprises multiple flow units that cooled as both simple and compound cooling units, and can be subdivided based on both cooling unit and flow unit stratigraphy (e.g., Smith and Bailey, 1966; Broxton and Reneau, 1995; Broxton et al., 1995a; Gardner et al., 1999, 2001) and crystallization characteristics (e.g., Broxton and Reneau, 1995; Broxton et al., 1995a). Below is a discussion of the stratigraphy, structural geology, and the potential for seismic surface rupture in the study area.

II. Previous Work

Previous geologic investigations within the study area include: geologic mapping and borehole studies for concerns regarding contaminant transport in Mortandad Canyon (Baltz et al., 1963); stratigraphic, borehole, and material property studies at Mesita de Los Alamos for facility siting (Purtymun, 1968); stratigraphic studies for waste management applications (Crowe et al., 1978); drilling test wells as part of the Environmental Restoration Project (e.g., Broxton et al., 1995b; Purtymun, 1995; Vaniman et al., in prep., Cole et al., in prep.); geology, stratigraphy, petrography, mineralogy, geomorphology, and fracture studies at TA-21 (Broxton et al., 1995a, 1995b; Goff, 1995; Reneau, 1995; Wohletz, 1995); geologic mapping (Goff, 1995; Reneau, 1995; Rogers, 1995); soil-stratigraphic studies of post-Bandelier tuff alluvial, colluvial, and volcanic deposits in Sandia Canyon (Reneau and McDonald, 1996); detailed geomorphic mapping in Los Alamos, DP, and Mortandad canyons (Reneau, 1995; Reneau et al., 1998b; Katzman et al., 1999; Drakos and Reneau, unpublished mapping); and detailed examination of deformation band faulting in nonwelded Tshirege Member unit Qbt3 at TA-53 (Wilson et al., 2001, 2002).

The general stratigraphic nomenclature for the Jemez volcanic field was developed by Bailey et al. (1969) and Smith et al. (1970). Smith and Bailey (1966) subdivided the Tshirege Member into five subunits that can be correlated throughout the volcanic field. Detailed studies in the area of Los Alamos (e.g., Broxton and Reneau, 1995; Gardner et al., 1999, 2001; Lewis et al., 2002) have resulted in subdivisions that are more applicable and useful for the local area. The stratigraphy of the Bandelier Tuff that was summarized and described by Broxton and Reneau (1995), based on studies in the eastern and central portions of LANL, is generally employed by geologists working on the Pajarito Plateau, with modifications to stratigraphy based on lateral variations within the units across LANL (e.g., Gardner et al., 1998, 1999, 2001; Lewis et al., 2002). Complexities in stratigraphic nomenclature within the Tshirege Member arise because of lateral variations in flow and cooling units caused primarily by thickness and temperature variations with distance

from the source (e.g., Gardner et al., 1999, 2001; Lewis et al., 2002). All previous work in the study area documents that the Tshirege Member units exposed are units Qbt1 to Qbt3, although they are subdivided and named differently by different workers (Figure 4; Baltz et al., 1963; Purtymun, 1968; Crowe et al., 1978; Broxton et al., 1995a, 1995b; Goff, 1995; Rogers, 1995); for example, Rogers (1995) uses units QbtA to QbtD, rather than Qbt1 to Qbt3.

Within the study area, the Otowi Member of the Bandelier Tuff and the Cerro Toledo interval are exposed only in Los Alamos Canyon and have been described in detail by Broxton et al. (1995a) and Goff (1995) in the TA-21 area. Thickness of the Otowi Member across LANL is highly variable because it was deposited on an irregular paleotopographic surface (Broxton and Reneau, 1996) and underwent about 400,000 years of erosion prior to deposition of the Tshirege Member. The thickest section of the Otowi Member encountered near the study area (130 m) was reported in Baltz et al. (1963) from borehole TH-8 in Mortandad Canyon. Borehole LADP-4 in DP Canyon penetrated 85 m (278 ft) of Otowi Member, including 8.5 m (28 ft) of the basal Guaje pumice bed (Broxton et al., 1995b). The Cerro Toledo interval (e.g., Broxton and Reneau, 1995; Broxton et al., 1995a) includes primary and reworked tephras of the Cerro Toledo Rhyolite (Smith et al., 1970), erupted from the Toledo caldera, and alluvial deposits derived from the Sierra de los Valles highlands to the west of the study area. The amount of primary volcanic deposits and alluvial gravels is highly variable depending on location. Exposures of the Cerro Toledo interval exposed in the study area are described in detail in stratigraphic sections OU1106-STRAT-1, 2, and 3 measured by Broxton et al. (1995a).

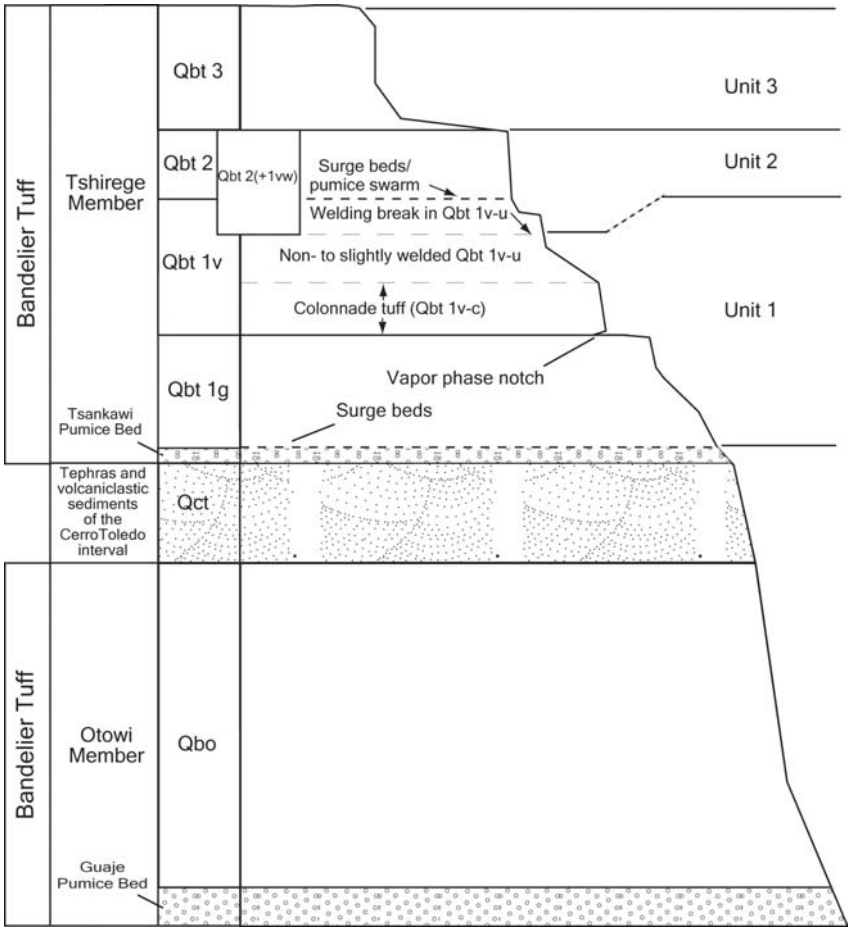

Figure 3. Generalized stratigraphy of lower units of the Bandelier Tuff and Cerro Toledo interval exposed in the study area (modified from Broxton and Reneau, 1995). Thickness of units is shown schematically and varies over the Pajarito Plateau. Unit Qbt2 to the west (e.g., Gardner et al., 1999) is equivalent to Qbt2(+1vw) in the western part of our study area, which includes unit Qbt2 and the upper part of Qbt1v-u in the eastern part of the study area. Unit designations are the same as on Plate 1.

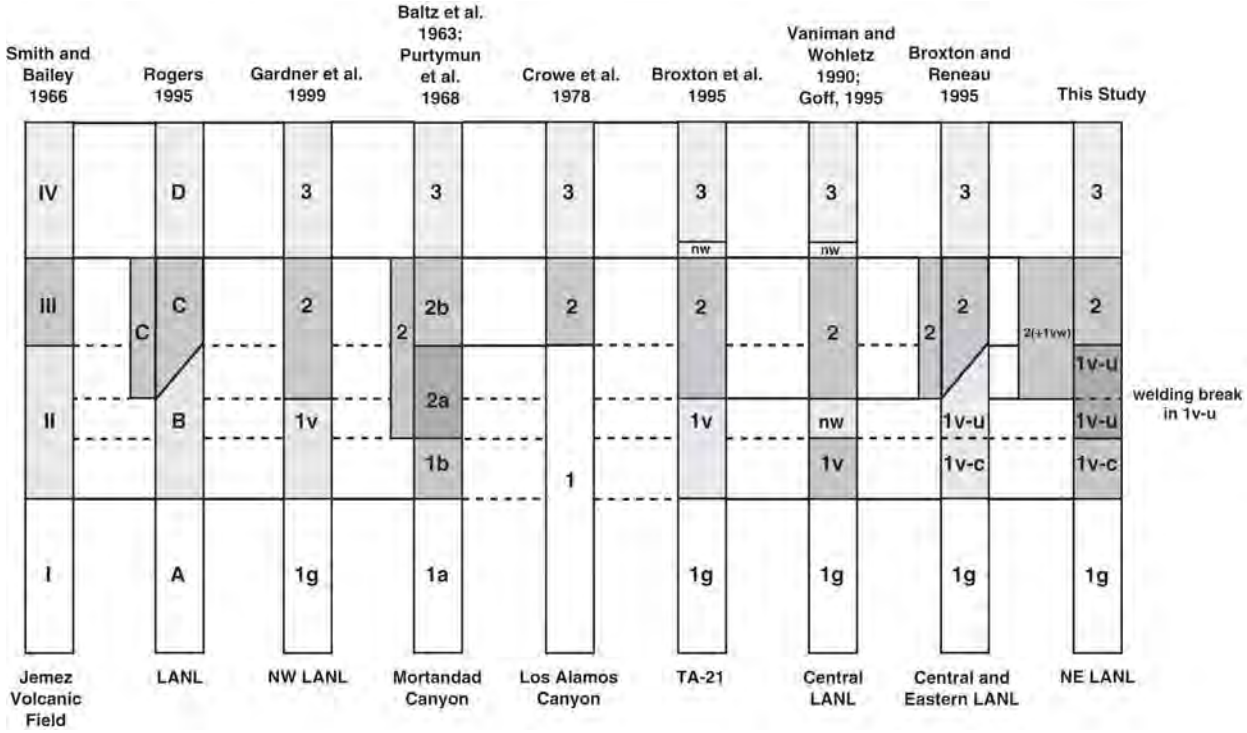

Figure 4. Comparison of stratigraphic nomenclature of subunits within the lower portion of the Tshirege Member of the Bandelier Tuff, as used in this report, to nomenclature used by previous investigators (modified from Broxton et al., 1995a). Diagonal lines in unit Qbt2 and QbtC indicate inconsistent placement of the unit Qbt1–Qbt2 contact.

Exposures of older alluvial deposits (Qoal) in DP Canyon are the type locality for Qoal, and have been described in detail by Reneau (1995). Canyon-bottom alluvial deposits (Qal) and terrace deposits (Qt) have been studied in detail in Sandia, Los Alamos, Mortandad, and DP canyons. Based on work in the study area and in other canyons on the Pajarito Plateau (e.g., McDonald et al., 1996; Reneau and McDonald, 1996; Reneau et al. 1996a; Reneau 2000), Qt has a probable age range from late Pleistocene to late Holocene. An approximately 4-m-thick sequence of alluvial and colluvial deposits exposed in Sandia Canyon (Plate 1, soil profile), and described by Reneau and McDonald (1996, pp. 40–46), indicates that the Qal+Qt sequence (Plate 1) in this area can locally exceed 80–110 ka in age [based on soil development below a 1.15-m (3.7 ft)-thick section of the El Cajete pumice, which was erupted from the El Cajete vent in the Valles caldera at ~50–60 ka (Toyoda et al. 1995; Reneau et al., 1996b)]. Available data indicate that much of the alluvium in the study area is Holocene in age (Reneau et al., 1996a; Reneau and McDonald, 1996, pp. 46–47), and in some cases post-dates 1942 AD (Reneau et al., 1998b; Katzman et al., 1999; Drakos and Reneau, unpublished mapping). In DP Canyon, alluvium, colluvium, and terrace deposits have a range of ages as shown by stratigraphic relations and several radiocarbon dates that range from ~37 ka to 2 cal ka (Reneau, 1995).

Evidence for faulting in the study area was first documented by Purtymun (1968), who mapped a fault at the future site of the Los Alamos Neutron Science Center (LANSCE; Plate 1) with 4.3 m (14 ft) of down-to-the-east displacement on the unit Qbt2–Qbt3 contact based on borehole data. Cross sections of Purtymun (1968) show displacement based on two boreholes (TH-8 and TH-9), which are approximately 1 km (0.6 miles) apart. Prior to development of the area, this fault was recognizable by a 15–45 cm (6–18 inch) wide gouge zone that stood approximately 1 m (2–3 ft) above the mesa surface and was about 6 m (20 ft) long (Purtymun, 1968). This fault has more recently been studied in detail by Wilson et al. (2001, 2002) to better understand deformation mechanisms of faults in nonwelded units of the Bandelier Tuff. The fault consists of closely spaced deformation bands caused by crushing of grains in the nonwelded tuff; this type of feature is a common

result of faulting in unlithified sediments and nonwelded tuffs (Wilson et al., 2001, 2002). Geologic mapping by Rogers (1995) shows no faults within the study area. Mapping by Goff (1995) in the area of TA-21 also shows no faults within the area; however, Wohletz (1995) recognized a ~500-m (~1600-ft)-wide fracture zone near Material Disposal Area (MDA)-V (Plate1, Figure 2) with a greater abundance and width of fractures in unit Qbt2 than in adjacent exposures. Fracture mapping by Wohletz (1995) was done on photographs of cliff faces and involved measurements of the density, strike, and aperture of fractures that may be associated with fault zones or constitute enhanced pathways for contaminants. Reneau et al. (1998a) performed detailed total station surveys of surges at and near the Qbt1v–Qbt2 contact in the area of TA-54 on Mesita del Buey, approximately 1.6 km (1 mile) to the south of the central part of our study area (Figure 2, location c), to assess structure in support of studies of contaminant transport. Their survey found 37 faults with 5–65 cm (0.1–2.1 ft) of vertical displacement on surges at the Qbt1v–Qbt2 contact on the north wall of Pajarito Canyon, extending approximately 1.6 km (1 mile) east of location c on Figure 2. Faults in the west end of the surveyed area at TA-54 (Figure 2) form two grabens and have the greatest amount of vertical displacement [~1–2 m (3.2–6.5 ft) per fault on surges at the Qbt1v–Qbt2 contact]. They inferred that these structures were associated with distributed deformation during paleoseismic events and that they do not represent a major fault zone. Faults mapped at TA-54 have a wide range of orientations and sense of offset, and form several horst and graben structures. Additionally, Dransfield and Gardner (1985) and Gardner and House (1987) show inferred buried faults within the study area (Figure 2) that are based on boreholes and geophysical studies.

The study area also appears to lie within the Velarde graben, a subsurface pre-Bandelier Tuff depression that may represent an area of hanging wall deformation associated with development of the western margin of the Rio Grande rift in the area of Los Alamos (Dransfield and Gardner, 1985; Broxton and Reneau, 1996). The western margin of the Velarde graben is defined by the Pajarito fault zone; the eastern margin is defined by the easternmost subsurface structure shown on Figure 2, and is inferred from geophysical evidence (Dransfield and Gardner, 1985). Further evidence for a north-northeast-trending subsurface depression comes from various geophysical and geological investigations. Budding (1978) identified a prominent gravity low about 3 km (1.9 mi) east of the city of Los Alamos and interpreted a north-northeast-trending graben in the subsurface that ranges from about 5 km (3.1 mi) to about 7 km (4.4 mi) wide. He interpreted the graben as partly syn-depositional and partly post-depositional with the Santa Fe Group, which he modeled as up to 2 km (1.3 mi) thick in the graben. Electromagnetic sounding surveys also defined a northeast-trending trough beneath the Pajarito Plateau (Williston, McNeil, and Associates 1979) in a similar location. Fergusson et al. (1995) interpreted a gravity low on the west side of the Española Basin as corresponding to thick sedimentary sequences accumulated in a graben. Broxton and Reneau (1996) subsequently noted that this gravity low might correlate with a large, Pliocene, pre-Bandelier Tuff valley, known from deep boreholes, that underlies the area (Figure 2).

III. Methods

A. Geologic Mapping

Geologic mapping was done on topographic base maps at a scale of 1:1,200, with 2-ft contour lines. Contours were derived from a digital elevation model (DEM), with a 4-ft grid, based on a laser altimetry or LIDAR (light detection and ranging) survey performed on the Pajarito Plateau in June 2000 (Carey and Cole, 2002). This base map derived from the LIDAR survey was chosen because it allows for identification of more subtle topographic features on the ground, and therefore more accurate placement of geologic contacts with relation to topography than would be possible using previous topographic base maps. Comparison of the LIDAR survey with GPS (Global Positioning System) and total station surveys (e.g., Gardner et al., 1999; Katzman et al., unpublished survey data) reveals that >90% of the LIDAR data has better than 2-ft horizontal position and better than 1-ft vertical position relative to GPS and total station survey data (Carey and Cole, 2002), which meets national map standards. Vertical inaccuracies in the LIDAR survey are largest and most common on steep slopes and cliffs and in heavily vegetated areas. Upon completion of mapping, field geologic maps were digitized, and the geologic map (Plate 1) was created using ArcMap computer software (© ESRI).

Stratigraphic units of the Bandelier Tuff and Cerro Toledo interval in this report are based on stratigraphic nomenclature presented by Broxton and Reneau (1995), with minor modifications to describe lateral stratigraphic variations within the Tshirege

Member. Surficial geologic units mapped are simplified and partially derived from previous investigations that included mapping and soil pits on the Pajarito Plateau (e.g., Reneau, 1995; Reneau et al., 1996a, 1996b, 1998b; Reneau and McDonald, 1996; Katzman et al., 1999). Detailed geomorphic mapping of the TA-21 area and portions of Los Alamos and DP Canyons can be found in Reneau (1995), Reneau et al. (1998b), and Katzman et al. (1999). Large parts of the map area have been disturbed by human activities or covered by artificial fill, buildings, and parking lots, partially obscuring original geologic relations.

B. Structural Analysis

Cooling and flow unit contacts in the upper units of the Tshirege Member have been used as stratigraphic marker horizons in previous seismic hazards studies to determine vertical displacement and the potential for seismic surface rupture along faults of the Pajarito fault system (e.g., Gardner et al., 1998, 1999, 2001; Lewis et al., 2002). Changes in vapor-phase crystallization and devitrification, often related to cooling and degassing, can form discrete, mappable zones within ignimbrites (Cas and Wright, 1987). Unit Qbt1 of the Tshirege Member, exposed in the central and eastern parts of LANL, is largely nonwelded, but has distinctive crystallization (and therefore weathering) characteristics that are mappable throughout the study area. Although changes in welding and crystallization mapped in this study and previous seismic hazards investigations around LANL are not necessarily stratigraphic features, they essentially coincide with or parallel stratigraphic contacts, providing large-scale, fairly planar markers for structural offset. Most contacts mapped in this study have been walked in their entirety and provide a strong basis for interpretations of geologic structures and their spatial relations.

Stratigraphic units are typically well exposed on south-facing cliffs, and are generally covered by colluvium and vegetation on north-facing slopes. Faults and related structures are in many cases easily recognizable on well-exposed cliffs; however, broad zones of distributed deformation on small-displacement faults can be subtle or unrecognizable in the field. Many of these broad zones of deformation can be recognized as changes in orientation of bedding through detailed 2-D and 3-D analysis of contact elevations in profiles, cross sections, and structure contour maps (e.g., Gardner et al., 1998, 1999, 2001; Lewis et al., 2002). To obtain 3-D data, digitized lines from field maps were converted to points every 20 ft, and x-y-z coordinates for these points were obtained from the 2000 LIDAR DEM (4-ft grid) using ArcGIS© computer software and its extensions. These data were then used to construct geologic cross sections (Plate 2), profiles, and three-dimensional surface diagrams using a variety of software packages. Inaccuracies in the DEM, especially on cliff faces, and the process of digitizing can result in some anomalous or spurious point elevations. However, it is usually easy to distinguish large irregularities imparted by the topographic base from geologic structures by checking these locations in the field. Three-dimensional surface models of selected geologic surfaces were interpolated using kriging (a linear regression technique for minimizing the variance of unsampled values between points; Deutsch and Journel, 1992) in the computer software Surfer© and were then contoured to examine anomalies and trends in surfaces. Surfaces were interpolated using a 500-ft grid spacing to minimize anomalies caused by the software in areas of no data and anomalies derived from inaccuracy of elevation data on cliff faces (partly caused by the scale of mapping, limitations of LIDAR data on cliff faces, and inaccessibility of outcrops on cliff faces). Grids interpolated using Surfer were then imported into ArcGIS for examination with relation to buildings, roads, and geologic structures. Cross sections were created using Terramodel© computer software and ArcGIS extensions Spatial Analyst and 3D Analyst, and contact elevations were derived from elevations of interpolated surfaces along the lines of cross section.

C. Mineralogy, Petrography, and Geochemistry

Samples of Bandelier Tuff were collected from four measured stratigraphic sections in Sandia and Mortandad canyons (Plate 1) for whole-rock X-ray diffraction (XRD), petrographic, and whole-rock X-ray fluorescence (XRF) analyses to support unit identification and stratigraphic correlations (see, for example, Broxton et al., 1995a; Gardner et al., 1999, 2001; Lewis et al., 2002). No sections were measured in Los Alamos Canyon because Broxton et al. (1995a) measured, described, and sampled three stratigraphic sections in the TA-21 area (Plate 1). Previous investigators (e.g., Broxton et al., 1995a) have demonstrated that whole-rock XRD analyses are useful in discriminating among lower units in the Tshirege Member. Whole-rock XRF analyses are not as useful in discriminating among the lower units of the Tshirege Member, but do show some variation with stratigraphic height (Broxton et al., unpublished data).

A total of 49 samples were collected from an outcrop depth of 5 to 10 cm (2–4 in.) to avoid obvious weathering rinds. Sample locations were mapped in the field using a hand level and topographic maps and are shown on Plate 1 and in Appendix A (Figures A1–4). Northing, easting, and elevation coordinates for sample locations were derived from the 2000 LIDAR DEM.

XRD analyses were performed on all 49 samples to characterize mineralogy of the samples; results are tabulated in Appendix B. Samples were first powdered in a tungsten-carbide shatter box, and then a small portion of each sample (~0.8 g) was mixed with 1.0-μm corundum (Al_2O_3) internal standard in the ratio 80% sample to 20% corundum by weight. Each sample was then ground under acetone in an automatic Retch Micro-Rapid mill (fitted with an agate mortar and pestle) for a time greater than 10 minutes. This produced a sample with an average particle size of less than 5 μm and ensured thorough mixing of sample and internal standard. All diffraction patterns were obtained on a Siemens D500 X-ray powder diffractometer using CuKa radiation, incident- and diffracted-beam Soller slits, and a Kevex Si(Li) solid-state detector from 2°–70°2θ, using 0.02° steps, and counting for at least 2 seconds/step.

Quantitative XRD analyses were conducted using the FULLPAT method and software (Chipera and Bish, 2002). FULLPAT is a quantitative XRD methodology that merges the advantages of existing full-pattern fitting methods with the traditional reference intensity ratio (RIR) method. FULLPAT is based on the premise that patterns for each individual phase in a mixture can be added in the correct proportions to reproduce the observed pattern. Like the Rietveld and other full-pattern quantitative analysis methods, it uses complete diffraction patterns, including the background. However, FULLPAT can explicitly analyze all phases in a sample, including partially ordered or amorphous phases such as glasses, clay minerals, or polymers. The addition of an internal standard to both library standards and unknown samples eliminates instrumental and matrix effects and allows unconstrained analyses to be conducted by the direct fitting of library standard patterns to each phase in the sample. FULLPAT makes use of a least-squares minimization routine to fit standard patterns to the observed patterns, thereby reducing user intervention and bias. FULLPAT has been coded into Microsoft EXCEL computer software using standard spreadsheet functions.

Petrographic thin sections of 46 samples were made to determine the constituents of samples for comparison with petrographic descriptions by Broxton et al. (1995a). Thin sections were examined for size and abundance of minerals and pumice and degree of devitrification and vapor-phase alteration to strengthen stratigraphic correlation of subunits in the Tshirege Member.

Major and trace elements were analyzed in 49 bulk samples using an automated Rigaku wavelength-dispersive XRF spectrometer. Variations in whole-rock geochemistry obtained by XRF analysis, especially variations in SiO_2 and TiO_2, have been proven useful for differentiating subunits within the upper part of the Tshirege Member (e.g., Gardner et al., 1999, 2001; Lewis et al., 2002). Results are compiled in Appendix C. Samples were first crushed and homogenized in 15–20-gram portions in a tungsten-carbide shatterbox in accordance with Yucca Mountain Project procedure LANL-EES-DP-130—Geologic Sample Preparation. Sample splits were dehydrated at 110°C for 4 hours and then allowed to equilibrate with ambient atmosphere for 12 hours. One-gram splits were fused at 1,100°C with 9 grams of lithium tetraborate flux to obtain fusion disks. Additional one-gram splits were heated at 1,000°C to obtain the loss-on-ignition (LOI) measurements. Elemental concentrations were calculated by comparing X-ray intensities for the samples to those for 21 standards of known composition, after correcting for absorption. The XRF method employed calculates the concentrations of ten major oxides (SiO_2, TiO_2, Al_2O_3, Fe_2O_3, MnO, MgO, CaO, Na_2O, K_2O, and P_2O_5), ten trace elements (V, Cr, Ni, Zn, Rb, Sr, Y, Zr, Nb, and Ba), and LOI (Appendix C). Elemental concentrations of V, Cr, and Ni in the Bandelier Tuff are generally below detection limits and therefore are not reported in Appendix C.

D. Notes on Units of Measure

Because the local Geographic Information System (GIS) and most of the LANL engineering databases are in the State Plane Coordinate System (New Mexico Central Zone, 1983 North American Datum) in feet, a mixture of English and metric units is used in this report. For maps and other geo-referenced figures, we employ English units. In all other cases, we use the metric system following general scientific practice. For length measurements at the centimeter scale or greater, English units are shown in parentheses adjacent to the metric length. For length measurements at the centimeter scale or less, measurements are shown only in metric units.

IV. Geology

A. Stratigraphy

Below are descriptions of stratigraphic units shown on the geologic map (Plate 1). We employ the stratigraphic nomenclature of Broxton and Reneau (1995) for the Bandelier Tuff with minor modifications to units Qbt1v and Qbt2 (Figures 3 and 4). For comparison, Figure 4 shows the approximate correlations of subdivisions of the Tshirege Member made by some authors for the Jemez Mountains and areas in and around Los Alamos, including stratigraphic nomenclature used in this report. The oldest exposed bedrock in the area is the 1.6-million-year-old Otowi Member of the Bandelier Tuff. Descriptions of the Otowi Member and Cerro Toledo interval are based largely on work by Broxton et al. (1995a).

Overlying the Bandelier Tuff are more recent alluvial and colluvial deposits, which have been mapped in detail by other authors (e.g., McDonald et al., 1996; Reneau and McDonald, 1996; Reneau et al., 1998b; Katzman et al., 1999; Drakos and Reneau, unpublished mapping), but are not subdivided in this report. Many areas within the study area, especially Mesita de Los Alamos (Plate 1), have been disturbed by human activities or are covered by artificial fill.

A.1 Otowi Member of the Bandelier Tuff (Qbo)

In the study area, the Otowi Member is exposed only in Los Alamos Canyon, and has been encountered in boreholes in Sandia and Mortandad canyons (e.g., Purtymun, 1995; Vaniman et al., in prep.; Cole et al., in prep.; Kuhn, in prep.; SAIC, unpublished data). The exposed portion of the Otowi Member in Los Alamos Canyon is 18–21 m (59–69 ft) thick, glassy, nonwelded and nonindurated, and has no apparent internal flow or cooling unit contacts. It consists of pumice lapilli, accidental lithics, and phenocrysts in a white to light grey-to-pinkish, ashy matrix. The matrix is made up of glass shards, broken pumice fragments, and fragments of perlite (Broxton et al., 1995a). Light grey-to-pinkish-orange glassy pumice lapilli make up 10%–40% of the tuff, with pumice content and size increasing toward the top of the unit. Pumice lapilli are 0.5 cm–6 cm (2.3 in.) in diameter and contain phenocrysts of bipyramidal quartz and sanidine. Phenocrysts of quartz and sanidine range in size from 0.5 to 2 mm and make up 7%–9% of the tuff. Trace amounts of clinopyroxene, plagioclase, and hornblende are also present. Accidental lithic fragments constitute 2%–5% of the upper part of the tuff, are 0.3 cm–3 cm (1 in.) in diameter, and are mostly derived from intermediate composition volcanic rocks of the Keres Group. Rare accidental lithic fragments derived from Tschicoma Formation dacite and Precambrian lithologies are also present (Broxton et al., 1995a).

A.2 Cerro Toledo interval (Qct)

In the study area, the Cerro Toledo interval is exposed in cliffs and slopes of Los Alamos Canyon and encountered in boreholes in Los Alamos, Sandia, and Mortandad canyons (Broxton et al., 1995b; Vaniman et al., in prep.; Kuhn, in prep.; SAIC, unpublished data). The interval exposed in the study area is 3–9 m (10–30 ft) thick and consists of primary and reworked tephras and alluvial gravels. The tuffaceous portion of the Cerro Toledo interval contains both primary pumice fall deposits and reworked ash and pumice. Reworked pumice includes both the typically aphyric pumice of the Cerro Toledo Rhyolite and reworked pumice derived from the Otowi Member of the Bandelier Tuff, which contains phenocrysts of quartz and sanidine. The unit includes alluvial sands and gravels that contain abundant Tschicoma dacite pebbles to boulders occurring in lenticular deposits that are 0.25–1.25 m (0.8–4.1 ft) thick in this area. Numerous buried soils within the sequence (McDonald, unpublished data) indicate several hiatuses in deposition.

A.3 Tshirege Member of the Bandelier Tuff (Qbt)

The stratigraphy of the Tshirege Member of the Bandelier Tuff as described in this report is shown in Figure 3. The degree of welding and crystallization in individual subunits of the Tshirege Member is described in detail at the four measured stratigraphic sections (Plate 3) and is generally consistent within each subunit throughout the map area. The degree of welding described for individual units is based on the flattening of pumice lapilli in hand specimen, and is consistent with welding characteristics described by Broxton et al. (1995a) for the Tshirege Member in the TA-21 area.

<u>Tsankawi Pumice Bed</u>: The Tsankawi pumice bed is the basal pumice fall of the Tshirege Member and ranges in thickness from 73 cm to ~1 m (2–3 ft) where exposed. The Tsankawi pumice consists of two pumice fall units separated by thin ash beds. The lower 60–74-cm (2–2.4 ft)-thick pumice bed consists of normally graded pumice lapilli in a matrix of phenocrysts and coarse ash. The two pumice beds are separated by two 2–7-cm (1–3 in.)-thick ashy beds made up of fragmented pumice lapilli, ash, and crystals. The upper pumice bed is 13–14 cm (~5 in.) thick and grades to ash at the top. The deposits

contain some hornblende-dacite pumice with minor amounts of clinopyroxene and plagioclase, and 1%–2% accidental lithic fragments of dacite that range in diameter from 0.5 cm–4 cm (1.5 in.; Broxton et al., 1995a). The Tsankawi pumice bed is exposed on the north side of Los Alamos Canyon and encountered in boreholes in the area.

Qbt1g: Unit Qbt1g ranges from 22–32 m (72–105 ft) thick. Qbt1g is the basal ignimbrite in the Tshirege Member and typically forms cliffy outcrops, especially near the top of the unit (Figures 5 and 6). The base of the unit is white and powdery, and the upper part is a dark pinkish-orange color and well indurated. The top of the unit is marked by a prominent notch or bench associated with a transition from glassy unit Qbt1g to the overlying vapor-phase-altered unit Qbt1v.

In the study area, the base of Qbt1g is exposed only in cliffs in Los Alamos Canyon. The base is marked in places by an ashy, pumice-poor, cross-bedded pyroclastic surge deposit that ranges in thickness from 10–25 cm (4–10 in.). The lower meter of the Qbt1g ignimbrite overlying the surge is typically ash-rich and pumice- and lithic-poor. Above this, unit Qbt1g is nonwelded, powdery, and white to the central portion of the unit. Qbt1g contains 15%–30% pumice lapilli, 1%–5% accidental lithic fragments, and 10%–20% phenocrysts. Pumice lapilli range from 3 mm to 15 cm (6 in.) in diameter and 3–5 cm (1–2 in.) in diameter on average. Pumice lapilli are white to light grey to pink, glassy, and fibrous, and contain 10%–15% phenocrysts of quartz and sanidine in subequal amounts. Minor amounts of hornblende-bearing pumice are also present. Accidental lithic fragments are mostly andesite and dacite, range in size from 2 mm to 5 cm (2 in.), and are mostly <5 mm in diameter. Lithic fragments decrease in size toward the top of the unit. Rare granitic lithic fragments also occur in Qbt1g (Broxton et al., 1995a). Phenocrysts are primarily quartz and sanidine in subequal amounts, with trace amounts of clinopyroxene, hornblende, and fayalite. The matrix and pumice lapilli in Qbt1g are largely glassy, but some devitrification and vapor-phase alteration is recognized, especially near the top of the unit, by axiolitic textures in minerals that have replaced glass shards and by tridymite crystals in some pumice lapilli. Glass shards are platy, blocky, and cuspate. The upper several meters of unit Qbt1g are more indurated, but nonwelded, bright orange, and mostly glassy.

The top of Qbt1g is marked by the uppermost occurrence of glass, with vapor-phase-altered tuff of unit Qbt1v-c above. This transition is usually gradational over about 10 cm (4 in.) to 1–2 meters (3–6 ft) and forms a prominent notch or bench, known as the vapor-phase notch (Crowe et al., 1978; Vaniman and Wohletz, 1990; Broxton et al., 1995a), which is a fairly continuous mappable marker horizon across the LANL site.

Qbt1v: Unit Qbt1v ranges from 30–40 m (100–130 ft) thick. We divide Qbt1v into two subunits: Qbt1v-c ("colonnade"; Broxton and Reneau, 1995) and Qbt1v-u ("upper"; Broxton and Reneau, 1995). Qbt1v-u has a nonwelded base, a partially to moderately welded center, and a nonwelded to moderately welded top. The base of the welded portion of Qbt1v-u is shown as a welding break within unit Qbt1v-u on Plates 1, 2, and 3 and Figures 3, 4, 5, 7, 8, and A1–4. We use the term "welding break" to describe a change in degree of welding [occurring over 1–2 m (3–6 ft)] that may or may not coincide with cooling or flow unit contacts. In the western part of the study area, the part of unit Qbt1v-u above the welding break is welded together with unit Qbt2 and is included in unit Qbt2(+1vw).

Qbt1v-c: The basal part of Qbt1v is a resistant "colonnade" tuff (Qbt1v-c) that has characteristic prominent vertical fractures that produce columns, distinguishing it from overlying Qbt1v-u. Qbt1v-c ranges in thickness from 3–7 m (10–23 ft); its upper contact with nonwelded unit Qbt1v-u is gradational over approximately 1 m (3 ft). Qbt1v-c either forms a continuous cliff with Qbt1g or forms steep outcrops above the bench formed by the Qbt1g–Qbt1v-c contact (Figures 5 and 6). Fracturing in the colonnade unit commonly extends down into unit Qbt1g. Qbt1v-c is typically nonwelded, light pink-orange, and indurated. It contains 20%–30% pumice lapilli, 10%–20% phenocrysts and 1%–5% accidental lithic fragments. Pumice lapilli are vapor-phase altered, grey to purple to brown, and range in size from 3 mm to 15 cm (6 in.). Pore spaces in pumice are filled with radiating, wedge-shaped crystals of tridymite, spherulites, blocky tridymite, and some primary sanidine phenocrysts. Most shards in the matrix have an axiolitic or microcrystalline texture. Shards are orange in plane light, and have darker, oxidized alteration rims. Alteration rims also occur around phenocrysts. Iron oxides occur as altered mafic minerals and cement in pore spaces and around shards. Quartz and sanidine phenocrysts are 1–2 mm in diameter. Accidental lithic fragments are up to 2 cm (~1 in.) in diameter. The matrix gets lighter in color and less indurated going up section. The unit becomes more difficult to recognize in westerly portions of the study area.

Figure 5. Photograph, looking north, of the Tshirege Member of the Bandelier Tuff exposed in Mortandad Canyon in the southeast portion of the study area. Moderately welded unit Qbt2 forms prominent cliffs where it overlies nonwelded unit Qbt1v-u.

Figure 6. Photograph, looking west, of units Qbt1g through Qbt2(+1vw) of the Tshirege Member of the Bandelier Tuff in Los Alamos Canyon in the northwestern part of the study area. The vapor-phase notch is visible between basal cliff-forming units Qbt1g and Qbt1v-c. The upper part of unit Qbt1v-u here is moderately welded and indistinguishable from unit Qbt2 in the upper cliffs.

Qbt1v-u: Qbt1v-u is 12–30 m (39–100 ft) thick and is a nonwelded to moderately welded, powdery, white, vapor-phase altered unit (Figures 5 and 6). The base of Qbt1v-u is marked by a decrease in induration from underlying Qbt1v-c. Unit Qbt1v-u contains 10%–20% pumice lapilli, 10%–15% phenocrysts, and <1%–3% accidental lithic fragments. Pumice lapilli are light grey to purple-brown, have a sugary texture, range in size from 2 mm to 8 cm (3 in.), and have an average size of 7 mm to 1 cm (2.5 in.). Approximately 10% of pumices are light gray and less vesicular and may contain hornblende. Accidental lithic fragments range from 4–6 cm (1.5–2.3 in.) in diameter and are generally larger to the west. Phenocrysts of quartz and sanidine are mostly 1–2 mm in diameter, with a maximum diameter of 4 mm. Pumice lapilli decrease in size and abundance going up section. Vapor-phase alteration of glass shards and pumice is evidenced by mostly blocky tridymite, with lesser amounts of wedge-shaped tridymite and sanidine in pore spaces. Shard and pumice morphology has been largely obliterated by alteration, but in some cases axiolitic texture can be seen. Some shards and pumice also display microcrystalline textures. Spherulites are rare.

Qbt1v-u in the eastern part of the study area is a cooling unit with a slope-forming, nonwelded base, and top and a central, partially to moderately welded, cliff-forming portion (Figure 5). There are several pumice swarms within Qbt1v-u, suggesting that it is made up of multiple pyroclastic flows. The base of the partially to moderately welded zone is shown on Figures 3 and 4 and Plate 1 as a welding break within Qbt1v-u and is gradational over 1–2 m (3–6 ft). In the eastern part of the study area, the contact between units Qbt1v and Qbt2 is both a cooling unit and a flow unit contact, marked by pyroclastic surges, pumice swarms, and a sharp upwards increase in welding from unit Qbt1v-u to Qbt2. To the west, the part of unit Qbt1v-u above the welding break is welded together with Qbt2 to form a compound cooling unit mapped as Qbt2(+1vw) (Plate 1 and Figure 6). Our combined unit Qbt2(+1vw) is equivalent to unit Qbt2 mapped by Broxton et al. (1995a) at TA-21 and unit Qbt2 mapped by Gardner et al. (1999) to the west of the study area.

Qbt2: Unit Qbt2 ranges in thickness from 2–25 m (6–82 ft). The greatest thickness of Qbt2 is in the western part of the study area and includes the upper welded portion of unit Qbt1v-u [i.e., Qbt2(+1vw)]. Unit Qbt2 is the most welded unit in the study area, and is generally a cliff-forming unit. Welding generally increases toward the top of the unit and to the west. The base of unit Qbt2 is commonly marked by a pumice swarm containing ~30% pumice lapilli up to 15 cm (6 in.) in diameter. This pumice swarm is generally <1 m (3 ft) thick. In the eastern part of the study area, the base of the unit is also marked by numerous pyroclastic surges [as documented by Reneau et al. (1998a) to the south and east of the study area].

Unit Qbt2 contains approximately 10%–15% vapor-phase-altered pumice lapilli, which range in size from <5 mm to 8 cm (3 in.) in diameter. The unit contains some white to light grey and less vesicular pumice lapilli, which may contain hornblende. Phenocrysts make up 15%–25% of the unit, with sub-equal amounts of quartz and sanidine up to 5 mm in diameter near the top of the unit, and some chatoyant sanidine. The unit contains <1%–2% accidental lithic fragments that are up to 3 cm (1 in.) in diameter but mostly <5 mm in diameter. Vapor-phase alteration of pumice and shards is evidenced by the presence of blocky and radiating tridymite in pore spaces, and axiolitic texture in glass shards. The top of Qbt2 is marked by a gradational decrease in welding [over 0.5–1 m (1.5–3 ft)] from moderately to partially welded unit Qbt2 to nonwelded unit Qbt3.

Qbt3: Unit Qbt3 ranges in thickness from 0–30 m (0–100 ft). The contact between underlying moderately welded Qbt2 and the nonwelded base of Qbt3 is a fairly sharp change in welding, from moderately welded to nonwelded, that occurs over less than 1 m (3 ft). Welding and induration increase slightly toward the top of the unit, making the upper part of Qbt3 a cliff-forming unit. Unit Qbt3 is distinct from underlying unit Qbt2 in that it contains more pumice lapilli, more crystals, generally larger crystals, and up to 5% accidental lithic fragments. The unit contains ~5%–20% vapor-phase-altered, grey pumice lapilli that are mostly ~1 cm, but as large as 15 cm (6 in.), in diameter. Pumice lapilli are vapor-phase altered throughout Qbt3, but are not as friable near the top of the section. Phenocrysts constitute 25%–35% of the unit, consist of quartz and sanidine in subequal amounts, and are 1–6 mm in diameter. Accidental lithic fragments constitute 3%–5% of the unit, and are up to 15 cm (6 in.) in diameter, but are mostly <5 cm (<2 in.) in diameter. Both the matrix and pumice are vapor-phase altered, and axiolitic texture is common in shards. Shard shapes and some tubular pumice textures are still preserved, but are mostly overprinted. Qbt3 forms the tops of most mesas in the western part of the study area. The overlying unit Qbt4 (e.g., Gardner et al., 1999) is not present in the study area, either because of erosion or nondeposition, and the original top of Qbt3 is eroded in places.

A.4 Older Alluvial Deposits (Qoal)

Older alluvial deposits (Qoal) within the study area consist of dacite-rich alluvium that was deposited on top of the Bandelier Tuff prior to and during the inception of major incision of present-day drainages (Reneau, 1995). These older alluvial deposits occur in Sandia Canyon, along an erosional bench along the edge of DP Mesa formed between moderately welded unit Qbt2 and nonwelded unit Qbt3, and in a small tributary to DP Canyon and (Plate 1). Qoal in the tributary to DP canyon was deposited against a stream-polished wall of unit Qbt3 and contains consolidated, stratified sands and gravels. Clasts are as large as 1 m (3 ft) in diameter and include stream-rounded gravels derived from Tschicoma Formation dacites exposed in the Sierra de los Valles (~20% of the clasts) and welded Tshirege Member units (~80% of the clasts; Reneau, 1995).

A.5 Recent Alluvial and Terrace Deposits (Qal+Qt)

In this report, recent alluvial deposits and terrace deposits are generally not broken out as separate units and are shown on Plate 1 as Qal+Qt. Unit Qal consists of relatively young alluvium along stream channels and includes presently active channels and adjacent floodplains, low terraces, and associated colluvium. Qal also includes active channel bottoms with little or no alluvium where exposed bedrock units were too small to break out as separate map units. Boreholes in Sandia and Mortandad canyons indicate the canyon bottom alluvium is as thick as 24 m (79 ft; Kuhn, in prep.). Unit Qt consists of stream terraces along the modern drainages and above the present canyon floors. Unit Qal+Qt includes coarse sand and gravel that represent bed-load sediment deposits, medium sand to silt deposits that represent overbank sediment deposits, and some colluvium derived from adjacent slopes.

A.6 Colluvium (Qc)

Unit Qc includes deposits on steep slopes that record primarily gravity-driven transport and deposits on gentle slopes that record deposition by surface runoff. Qc includes deposits that have a wide range in origin, texture, and age that were not practical to subdivide in this investigation. In addition, on many mesa tops, Qc includes fine-grained deposits that are probably dominated by eolian sediment, although this eolian sediment may be locally reworked by surface runoff and/or mixed with other material by bioturbation. Qc includes deposits that range in age from >50 to 60 ka (pre-El Cajete pumice) to present (Reneau, 1995). Small thin patches of colluvial cover that do not obscure underlying stratigraphic relations were generally not mapped and are included on Plate 1 in other map units. Where it was possible to determine the unit directly underlying Qc, it is shown on Plate 1 as “Qc/Qbt3”, for example, to indicate that thin colluvium overlies unit Qbt3.

A.7 Artificial Fill

Artificial fill and areas of anthropogenic disturbances are widespread in the map area. On Plate 1, this unit locally includes highly disturbed areas, such as roads, parking lots, and areas around buildings. Many areas that include patchy or thin fill were mapped as the underlying stratigraphic unit.

B. Mineralogy and Geochemistry of Tshirege Member Units

B.1 Mineralogy

Examination of thin sections and XRD analyses of whole-rock samples collected from measured stratigraphic sections (Plate 1, Appendix A) show that the Tshirege Member units Qbt1 through Qbt3 consist primarily of quartz + feldspar ± cristobalite ± tridymite ± glass (Appendix B, Figure 7). Hornblende, biotite, magnetite/maghemite, hematite, calcite, halite, and scapolite occur in minor amounts.

Glass is present in unit Qbt1g and the lower portions of Qbt1v-c and occurs as pumice lapilli and glass shards in the ashy matrix. Glass makes up 50%–70% of unit Qbt1g, but the abundance of glass drops off dramatically up section within 1–2 meters (3–7 ft) of the Qbt1g–Qbt1v-c contact. No glass is present in the measured sections (Plate 1) above unit Qbt1v-c (Figure 7). Feldspar occurs as phenocrysts in the matrix and pumices and microlites in pore spaces and along the edges of pumice and glass shards, and makes up 20%–60% of units Qbt1g to Qbt3. Feldspar abundance increases sharply from approximately 20% in Qbt1g to >60% in overlying units (Figure 7). Samples from units Qbt1g to Qbt3 contain 10%–30% quartz, which occurs as phenocrysts in the pumice and matrix. Although there are some variations, generally the abundance of quartz increases up section from unit Qbt1g to Qbt1v, then remains fairly constant through units Qbt1v, Qbt2, and Qbt3. Cristobalite constitutes 0%–15% of units Qbt1g to Qbt3, is greatest in abundance near the top of Qbt1v-c, and decreases upwards in unit Qbt1v-u (Figure 7).

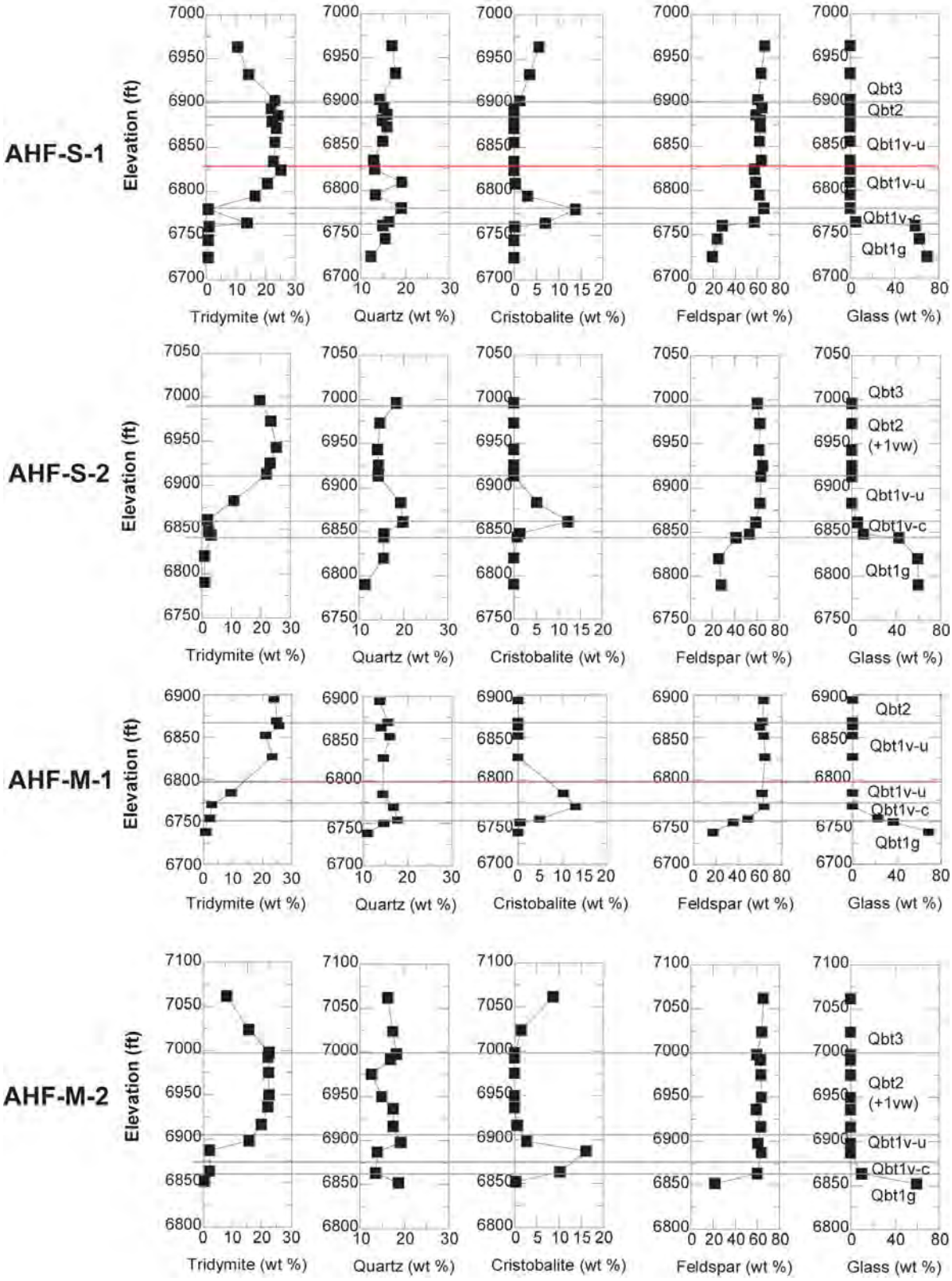

Figure 7. Variation diagrams showing mineralogy of tuffs in stratigraphic sections AHF-S-1, AHF-S-2, AHF-M-1, and AHF-M-2 in relation to elevation and mapped subunits within the Tshirege Member. Data are from XRD analysis of whole rock samples. Red line indicates the welding break in unit Qbt1v-u.

Cristobalite decreases to near 0% above the welding break in Qbt1v-u and in unit Qbt2, then increases to 5%–10% in Qbt3. Cristobalite occurs as axiolitic and spherulitic growths that have replaced the original glass shards in the matrix. Tridymite constitutes 0%–30% of units Qbt1g through Qbt3. Tridymite abundance varies inversely with cristobalite (Figure 7), and with the exception of a peak at the base of unit Qbt1v-c in section AHF-S-1, shows a sharp increase at the top of unit Qbt1v-c, increases upward within unit Qbt1v-u and Qbt2, and then decreases in unit Qbt3. The upper part of unit Qbt1v-u, generally above the welding break in unit Qbt1v-u, contains the highest abundance of tridymite in the Tshirege Member. Iron oxides are more abundant in Qbt1v-c than in overlying unit Qbt1v-u and occur as altered mafic phenocrysts, observable in thin section, as well as magnetite/maghemite microcrystals in shards (e.g., Schlinger et al., 1988; Stimac et al., 1996), and perhaps hematite cement in the matrix. Hornblende occurs primarily in unit Qbt1v as microphenocrysts in the matrix and in pumice.

B.2 Geochemistry of Tshirege Member Units

Results of XRF analyses of bulk rock samples from units Qbt1 through Qbt3 are tabulated in Appendix C. Variation of SiO_2 and TiO_2 with height in the stratigraphic sections is shown in Figures 8a and 8b. SiO_2 content in units Qbt1 through Qbt3 ranges from 73.0%–78.5%, and is generally lower in units Qbt1g and Qbt1v-c than in units Qbt1v-u, Qbt2, and Qbt3 (Figure 8a). Figure 8b shows a general increase in TiO_2 going up section from unit Qbt1g to Qbt3. Although there are variations in the SiO_2 and TiO_2 content between units, these variations alone are not distinct enough to use for differentiating units in this part of the Tshirege Member section (Figure 8).

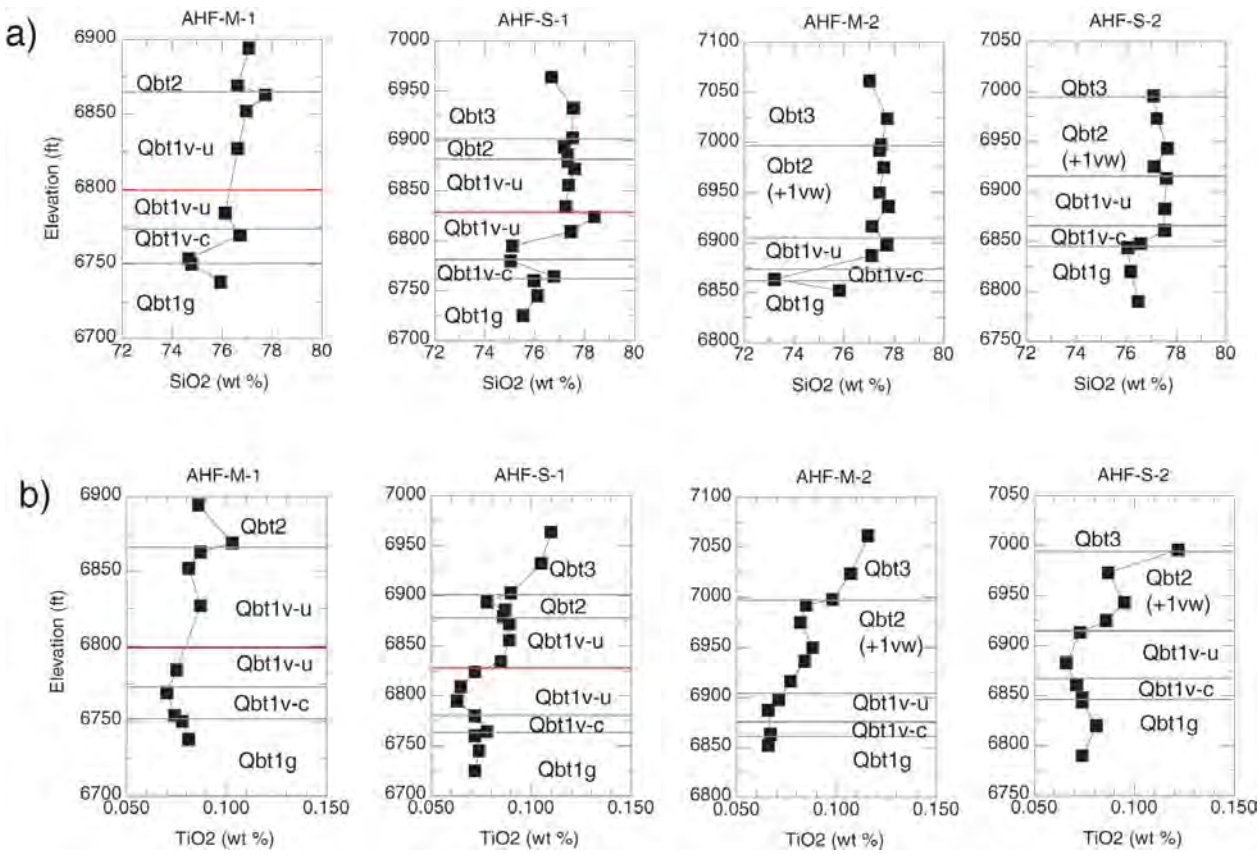

Figure 8. Major element oxide variation diagrams. Data are normalized from XRF analysis of whole rock samples. a) Plots show variation in weight percent SiO_2 vs elevation in stratigraphic section. The red line indicates the welding break in unit Qbt1v-u. b) Plots show variation in weight percent TiO_2 vs elevation. The red line indicates the welding break in unit Qbt1v-u.

C. Structural Geology

C.1 Faults

Field mapping revealed a few small displacement [<1.5 m (5 ft) of vertical displacement on stratigraphic markers in units Qbt1g to Qbt3] faults within the study area, but only four of these had clear evidence of offset on mapped contacts. Two zones of faulting and fracturing were identified in roadcuts of nonwelded unit Qbt3, and may not have been recognized without the excellent exposures. Although no stratigraphic markers are exposed in these zones to determine displacement, faulting is inferred based on cataclastic textures characteristic of faulting in nonwelded tuffs and poorly lithified sediments (e.g., Wilson et al., 2001, 2002). None of the faults or fracture zones can be traced laterally across mesa tops or canyons. Faults and fracture zones found in the study area are described below.

A fault exposed north of the beam line (building TA-53-3f) at LANSCE (Plate 1, F1) crops out in nonwelded, vapor-phase-altered unit Qbt3. This fault is unique in that its relatively complex fault-zone architecture is well preserved compared to other small-displacement faults in the area. The 15-to-20-cm-wide fault zone is oriented N16E, 82SE and consists of a discrete slip surface adjacent to a zone of densely spaced deformation bands (Figures 9a and 9b), which are visible in outcrop as nearly vertical planes of varying resistance to erosion. Deformation bands are distinct from fractures, which are common in Qbt2 and other, more welded units of the Bandelier Tuff, in that they have no discrete slip surfaces, but instead are tabular zones of grain-size reduced material and collapsed pore space. Each deformation band in fault F1 is an approximately 1-mm-wide zone of crushed phenocrysts and crystallized glass shards with reduced porosity (Figure 9c) compared to the Qbt3 protolith. The spatial density of these deformation bands increases from the eastern edge of the fault toward the western edge of the fault, where the anastamosing bands are deformed and truncated by an open, discrete slip surface (Figures 9a and 9b). Electron microprobe analysis indicates that the open slip surface of this fault has coatings of Fe- and Sn-oxide minerals (Figure 10); individual, undisturbed crystal faces can be seen on the slip surface. Fault F1 contains neither roots nor calcite. We found no evidence for dip slip displacement on stratigraphic markers based on mapping in adjacent Los Alamos and Sandia canyons, and the fault could only be traced a short distance along the mesa top in unit Qbt3. Though we cannot exclude strike slip offset, we could not document it.

An approximately 180-m (600-ft)-wide zone of abundant fractures and faults to the north of the aggregate G surface impoundments at TA-53 (referred to as “the lagoons”) is exposed in roadcuts of nonwelded, vapor-phase-altered unit Qbt3 (Plate1, F2). These fractures and faults deform roughly the same part of unit Qbt3 as fault F1. Approximately 150 fractures were counted within this zone. Orientation and width were measured for 71 of these; those with maximum widths <2 cm (<1 in.) were not measured because they are likely to be cooling joints that are typical in the Tshirege Member (Vaniman and Wohletz, 1990; Kolbe et al., 1994, 1995; Wohletz, 1995, 1996; Rogers et al., 1996). Maximum widths of measured fractures range from 2–60 cm (1 in.–2 ft); 70% have widths <10 cm (4 in.). Only the narrowest fractures in this zone are open, and most 1–2-cm (0.5–1 in.) wide fractures are filled with clay-sized material of unknown composition. Most wider fractures are filled with a mixture of ash, pumice, phenocrysts, and lithic fragments. Some are filled with fine-grained material and clasts of tuff (Figure 11a). Many fractures contain abundant roots and root mats, anastamosing clay seams, and abundant calcite that form tabular zones along one or both walls of the fracture or within the fracture filling (Figure 11b). Cross-cutting relations suggest multiple periods of formation of clay and calcite. Many of these fractures show a distinct foliated appearance with clay, calcite, and sparse vertically aligned lithic fragments defining the foliation. By analogy with fault F1, foliation could be associated with deformation band faulting; however, overprinting by clays, calcite, and roots make it difficult to determine the presence or absence of deformation bands, and no stratigraphic markers are exposed to determine displacement or lack thereof along individual fractures. The finer-grained material in these fractures could have resulted from grain size reduction due to cataclasis (e.g., Reneau and Vaniman, 1998) or infilling of open fractures from the surface. Some faults in this zone exhibit fracture-based morphologies rather than deformation banding. The most prominent of these is a zone about 60 cm (2 ft) wide that exhibits considerable brecciation of the host tuff (Figure 11c).

(a)

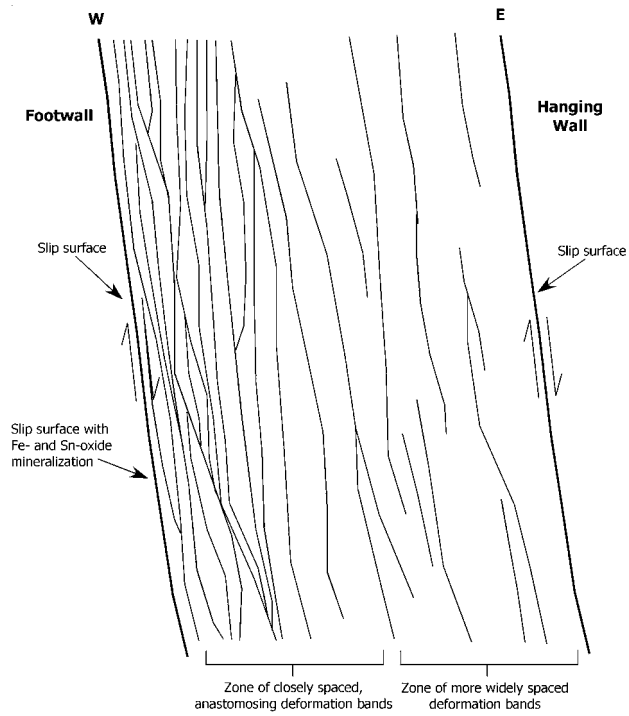

(b)

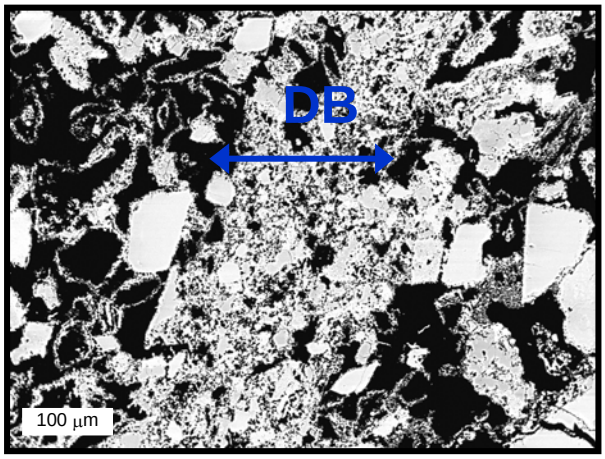

(c)

Figure 9. (a) Outcrop photograph of fault F1 showing the zone of deformation bands adjacent to an open, discrete slip surface. (b) Schematic diagram showing the structural elements of the 15–20-cm (6–8 in.)-wide fault zone. Down-to-the-east displacement is inferred based on the dip of the fault. (c) Back-scattered electron (BSE) microprobe image of a deformation band (labeled DB) from the eastern edge of the fault zone. Note the reduction in pore space (black) and the reduced size of phenocrysts, glass shards, and pumice fragments in the deformation band.

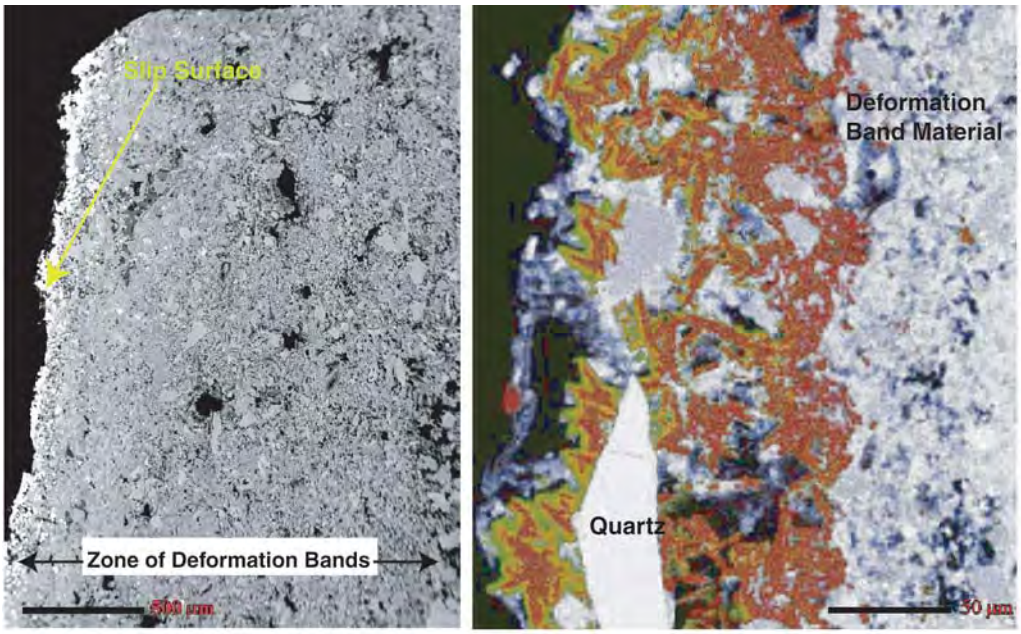

Figure 10. (a) Back-scattered electron image of the slip surface of fault F1, displacing the zone of deformation-band material. The slip surface is coated by high-atomic-number minerals (appearing white in this image) adjacent to a zone of deformation band material. (b) X-ray image of Fe- (red) and Sn-oxide (green) mineralization on the open slip surface shown in (a).

Figure 11a. Photograph of 15–20-cm (6–8 in.)-wide fracture or fracture-based fault in nonwelded, vapor-phase-altered unit Qbt3 north of the lagoons in fault zone F2, filled with fine-grained ash, pumice, lithics, and fragments of tuff. Pen for scale. Subhorizontal calcite band may be offset across the fracture, but many such adjacent calcite bands are highly irregular in shape.

Figure11b. Photograph of 15-20-cm (6–8 in.)-wide possible deformation band fault in nonwelded, vapor-phase-altered unit Qbt3 north of the lagoons in fault zone F2. Fracture is filled with foliated, fine-grained ash, lithics, pumice, and tuff fragments as well as roots, clay, and calcite. Possible shear fabric is heavily overprinted by roots and associated clay and calcite. Note pen for scale.

Figure 11c. Photograph of 60-cm (2 ft)-wide fracture-based fault north of the lagoons in fault zone F2. Brecciated tuff and open voids in the fault are visible adjacent to and below the hammer.

Geometric analysis using methods similar to Lewis et al. (2002) shows that the faults and fractures as a group have a statistically significant north-northeast preferred orientation (mean direction of N12E ± 26°, Fig. 12) and dip steeply (74°–90°), with a mean dip of 87 ± 5°. Despite some scatter in strike and dip, these data pass uniformity tests at the 95% confidence level, indicating that the data are derived from a population of structures with preferred orientation. It is possible, however, that the preferred orientation is biased by the orientation of the exposure (approximately E-W) as cautioned by Reneau and Vaniman (1998) for exposures at Area G..

Zone F2 lies north and slightly east of a 60-m (200-ft)-wide fault zone exposed in a tributary to Sandia Canyon (Plate 1, F3), which has approximately 1.2 m (4 ft) of down-to-the-northwest displacement exposed in units Qbt1g, Qbt1v-c, and Qbt1v-u (measured by leveling on the top of unit Qbt1g) across a 45-m (150-ft)-wide zone. The population of 11 faults measured within this zone shows no preferred orientation. Most of these faults are open slip surfaces with subvertical slickensides in welded units Qbt1v-u and Qbt2, but display cataclastic textures down-dip in nonwelded unit Qbt1v-u. Trace lengths appear to be short, most of these faults terminate at intersections with other faults or fractures. These faults appear to be caused by minor reactivation of cooling joints.

Three small down-to-the-west faults were found in the western part of the study area: fault F4 in a small tributary to Sandia Canyon that has ~1 m (2-3 ft) of down-to-the-west displacement on units Qbt1 to Qbt3, fault F5 in a roadcut near the guard gate at the entrance to LANSCE that has ~0.6 m (2 ft) of down-to-the-west displacement on the Qbt2–Qbt3 contact, and fault F6 on the western boundary of the study area that has ~1.5 m (5 ft) of down-to-the-west displacement on the Qbt2–Qbt3 contact (Plate 1).

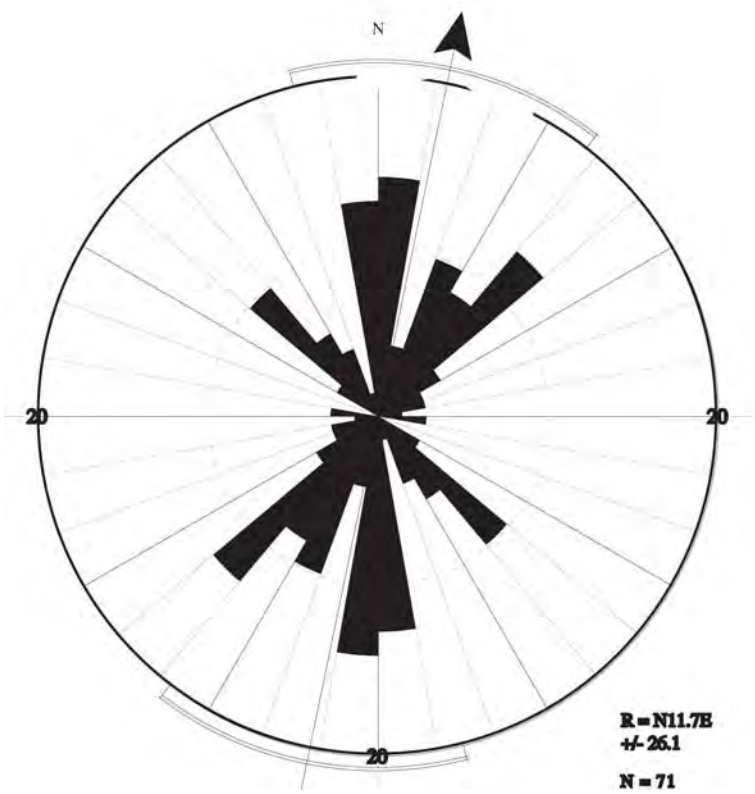

Figure 12. Rose diagram of strikes of fracture data from fault and fracture zone F2 exposed in approximately E-W trending roadcuts north of the lagoons. The inner circle represents 10% of the data analyzed, and the outer circle represents 20%. The mean strike, indicated by the arrow, is accompanied by the 95% confidence interval. Abbreviations: R, *resultant vector, or mean strike; N, number of measurements.*

C.2 Zones of Changes in Dip of Stratigraphic Markers

Units Qbt1g through Qbt3 strike approximately N15E and dip between 0.3º and 3.4º to the southeast. The average dip on all units across the study area is about 1.0º to the southeast. Three-dimensional surfaces defined by the tops of units Qbt1g to Qbt2 show consistent but subtle patterns of changes in dip on the order of 1º-2º (Figures 13a–13d). Three subparallel zones of changes in dip (steepening to the east) were recognized on the top of units Qbt1g, Qbt1v-c, Qbt1v-u, and Qbt2 (Figures 13a–13d). Based on the 3-D surface models, these zones trend approximately N10-15E, parallel to the general strike of bedding in this area. The westernmost zone is an increase in eastward dip of approximately 0.5º on the tops of Qbt1g and Qbt1v-c, but no changes in dip are apparent on the top of Qbt2; however, anomalies in the top of the Qbt2 surface exist in the northernmost part of the study area (Figure 13d). The central zone is an increase in eastward dip of ~2º on the top of Qbt1g, <1º on the top of Qbt1v-c, ~2º on the top of Qbt1v-u (this change occurs further south than on the tops of Qbt1g, Qbt1v-c, and Qbt2 and may not be a part of the same feature), and 0.8º on the top of Qbt2 (this change occurs further east on the top of Qbt2 than on the tops of Qbt1g, Qbt1v-c, and Qbt1v-u). The easternmost zone is an increase in eastward dip of ~1º on the tops of Qbt1g and Qbt1v-c, 0.6º on the top of Qbt1v-u, and 0.2º on the top of Qbt2 (however, data are sparse for the top of Qbt2 in this area, and a greater change in dip is apparent in the northeastern part of the area). Fault F1 coincides with the central zone of change in dip, and fault zones F2 and F3 coincide approximately with the eastern zone of change in dip. Although these dip changes are small in magnitude, they occur in approximately the same location in all units, and the magnitudes generally appear to decrease up section.

V. Discussion

A. Stratigraphy of Tshirege Member and Post-Bandelier Tuff Units

Tshirege Member stratigraphic units described in this report in the area of TAs 5, 53, 21, 73, and 72 include units Qbt1g, Qbt1v-c, Qbt1v-u, Qbt2(+1vw), Qbt2, and Qbt3. Detailed mapping of these units, based on variations in welding and crystallization, across the study area provided insight into how these units vary laterally and how they correlate to stratigraphy described by previous workers. Petrographic and geochemical data further support correlation of units to those previously described and reveal distinctive characteristics that are useful for differentiating units.

A.1 Comparison of Tshirege Member Units to Previous Studies

Tshirege Member units mapped and described in this study generally correlate with those described in previous geologic mapping, borehole, and stratigraphic studies (Figure 4). Some differences in placement of contacts between Plate 1 and previous maps are due to the scale of mapping and the accuracy of the topographic base maps used for mapping, and some are due to differences in stratigraphic nomenclature and criteria used to subdivide units. Variations in mineralogy (e.g., glass, tridymite, cristobalite, and feldspar content) and in devitrification and vapor-phase alteration textures, based on XRD analyses and characteristics of the units in thin section, are consistent with those of Broxton et al. (1995a).

Unit Qbt1g is recognized and broken out by most workers as a distinct glassy unit at the base of the Tshirege Member. Crowe et al. (1978) included both unit Qbt1g and Qbt1v in unit Qbt1, with no subdivision. Unit Qbt1g is directly correlative to unit QbtA of Rogers (1995).

The vapor-phase altered unit Qbt1v has been divided in a number of ways over the years. Our unit Qbt1v-c ("colonnade") correlates with unit Qbt1b of Baltz et al. (1963), unit Qbt1v of Goff (1995), and the colonnade unit (Qbt1v-c) of Broxton and Reneau (1995) and Broxton et al. (1995a, 1995b). Unit QbtB of Rogers (1995) includes our units Qbt1v-c and Qbt 1v-u. Our petrographic observations of devitrification and vapor-phase alteration minerals and textures in Qbt1v are consistent with those of previous investigators.

The recognition of a mappable welding break within unit Qbt1v-u, and inclusion of the upper welded part of Qbt1v-u in unit Qbt2(+1vw) in the western part of the area is helpful in clarifying inconsistencies as to how the Qbt1–Qbt2 contact has been previously mapped or described. In the eastern part of LANL, the Qbt1v–Qbt2 contact has generally been placed at a flow and cooling unit contact (Reneau et al., 1998a) that is commonly marked by pyroclastic surges, pumice swarms, and an upward increase in welding (Figure 5). In the central to western portions of LANL, the Qbt1v–Qbt2 contact has generally been placed at a gradational upwards increase in welding (e.g., Broxton et al., 1995a),

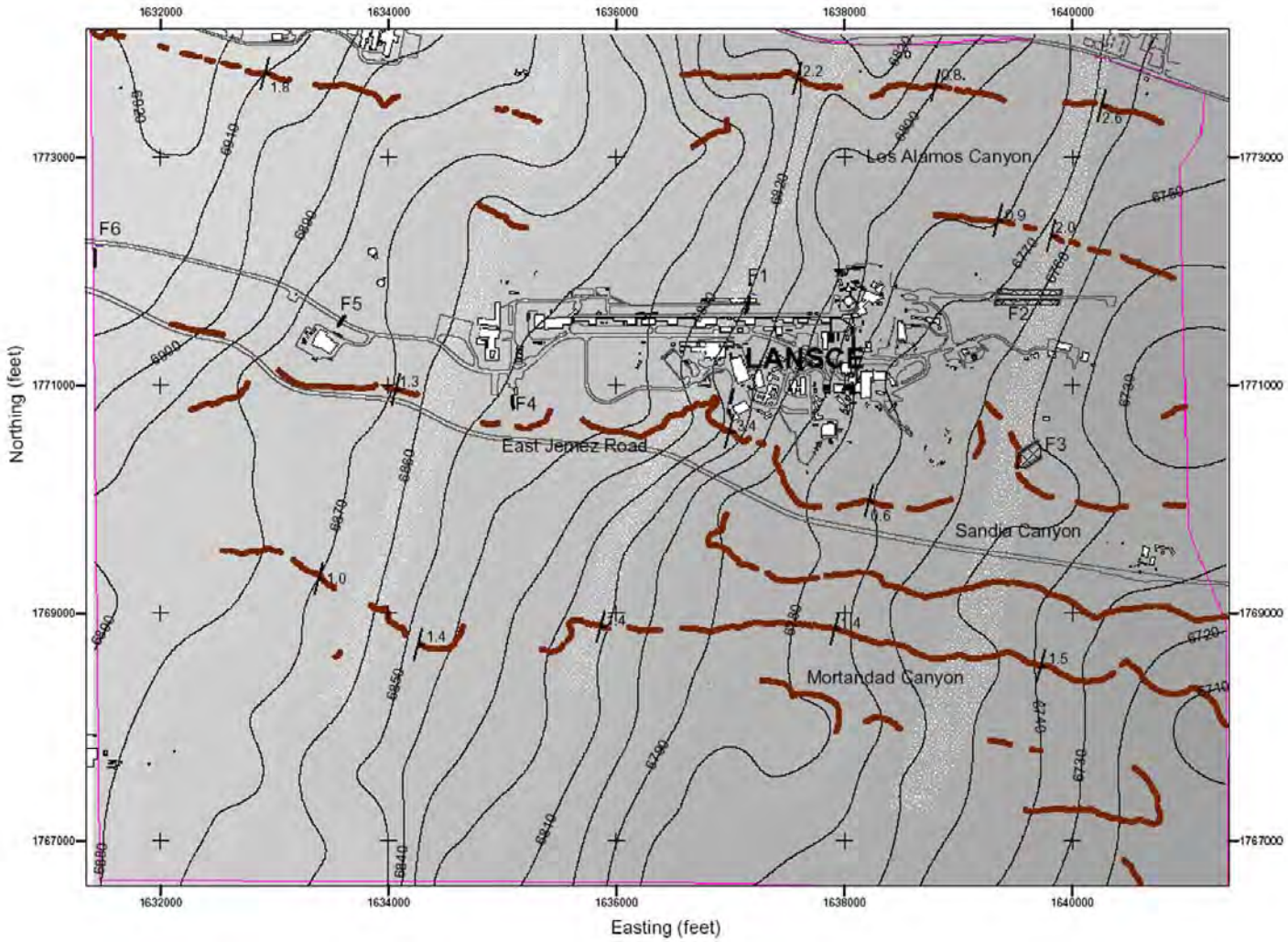

Figure 13a. Contoured upper surface of unit Qbt1g. Points are derived from the mapped unit Qbt1g–Qbt1v contact (see text for methods). Faults are shown as thick black lines. Fault and fracture zones are cross-hatched and are bounded by thick gray lines representative of average strikes or the edge of the zone. The white stipple pattern indicates areas of change in dip (eastward steepening). Elevations of points were derived from the 4-ft grid, 2000 LIDAR DEM (Carey and Cole, 2002). The surface was interpolated using kriging with a 500-ft grid spacing; the contour interval is 10 ft. The grid is in the State Plane Coordinate System, New Mexico Central Zone, 1983 North American Datum (in feet). The surface model is constrained by mapped contact elevations; in some areas of limited or no data, the software creates spurious topography. Structural features, strike and dip, and buildings are labeled as on Plate 1.

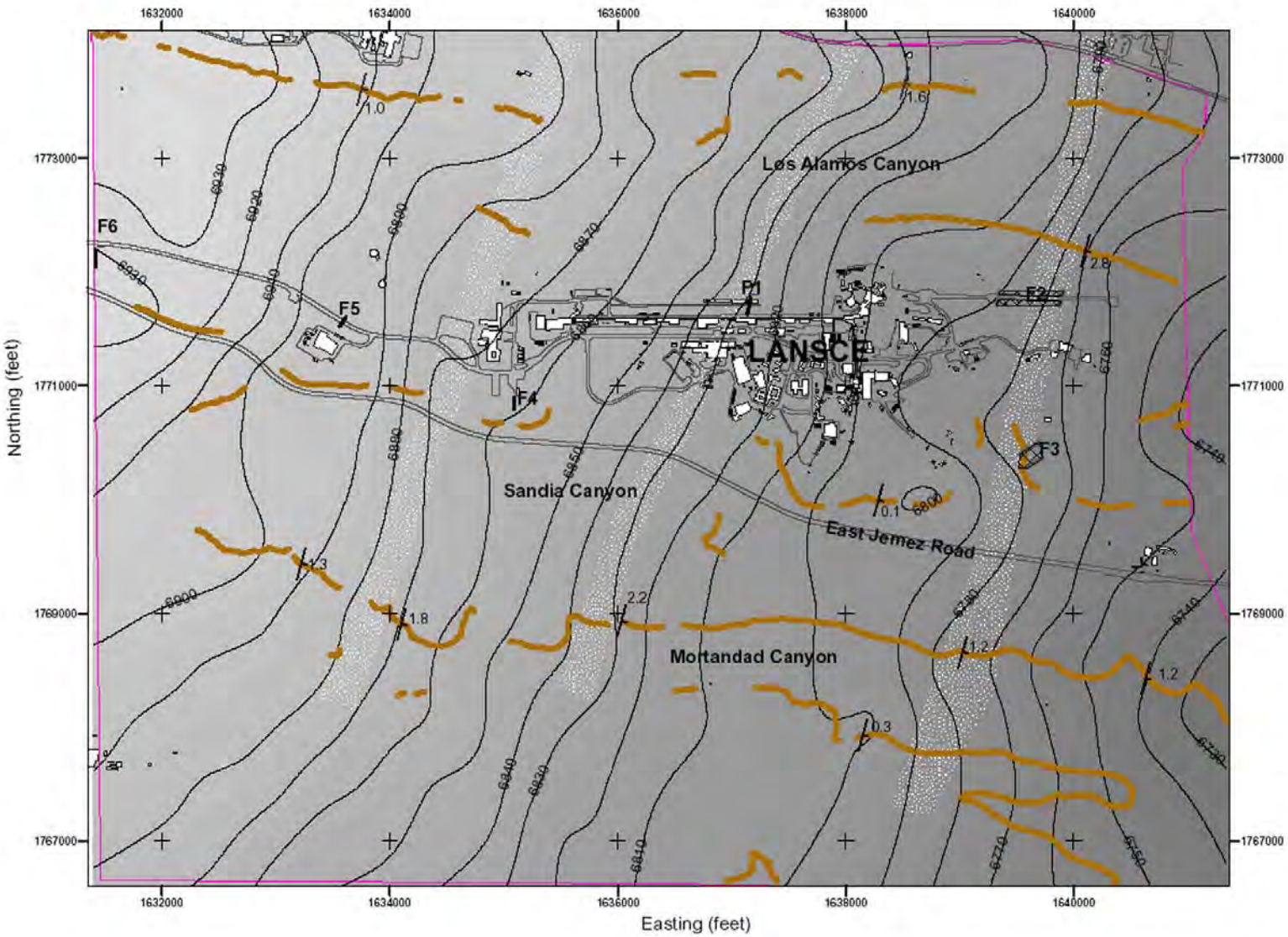

Figure 13b. Contoured upper surface of unit Qbt1v-c. Points are derived from the mapped unit Qbt1v-c–Qbt1v-u contact. Methods for generating this surface, contour interval, labeling, and uncertainties are as in Figure 13a.

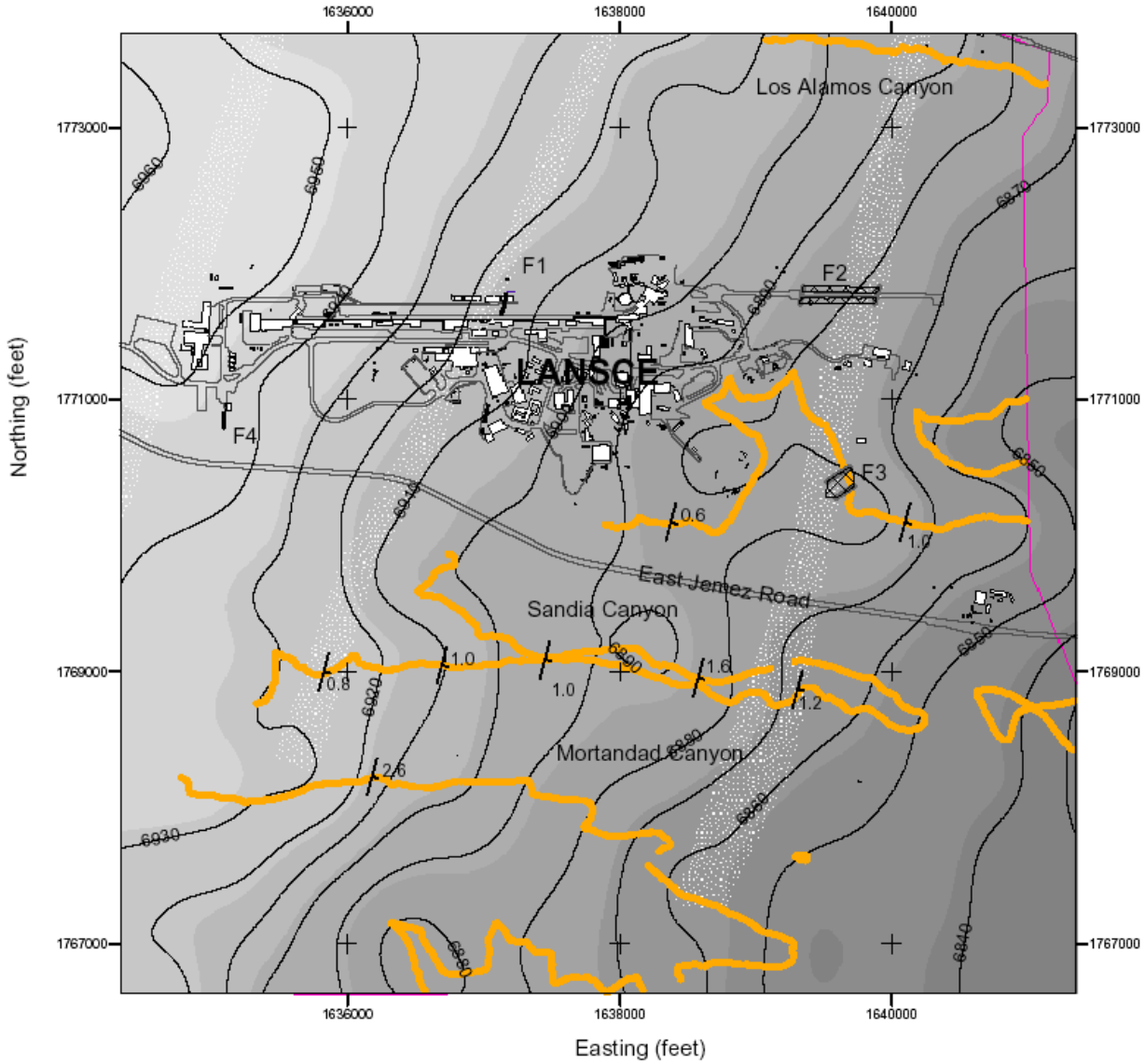

Figure 13c. Contoured upper surface of unit Qbt1v-u. Points are derived from the mapped unit Qbt1v-u–Qbt2 contact. Methods for generating this surface, contour interval, labeling, and uncertainties are as in Figure 13a.

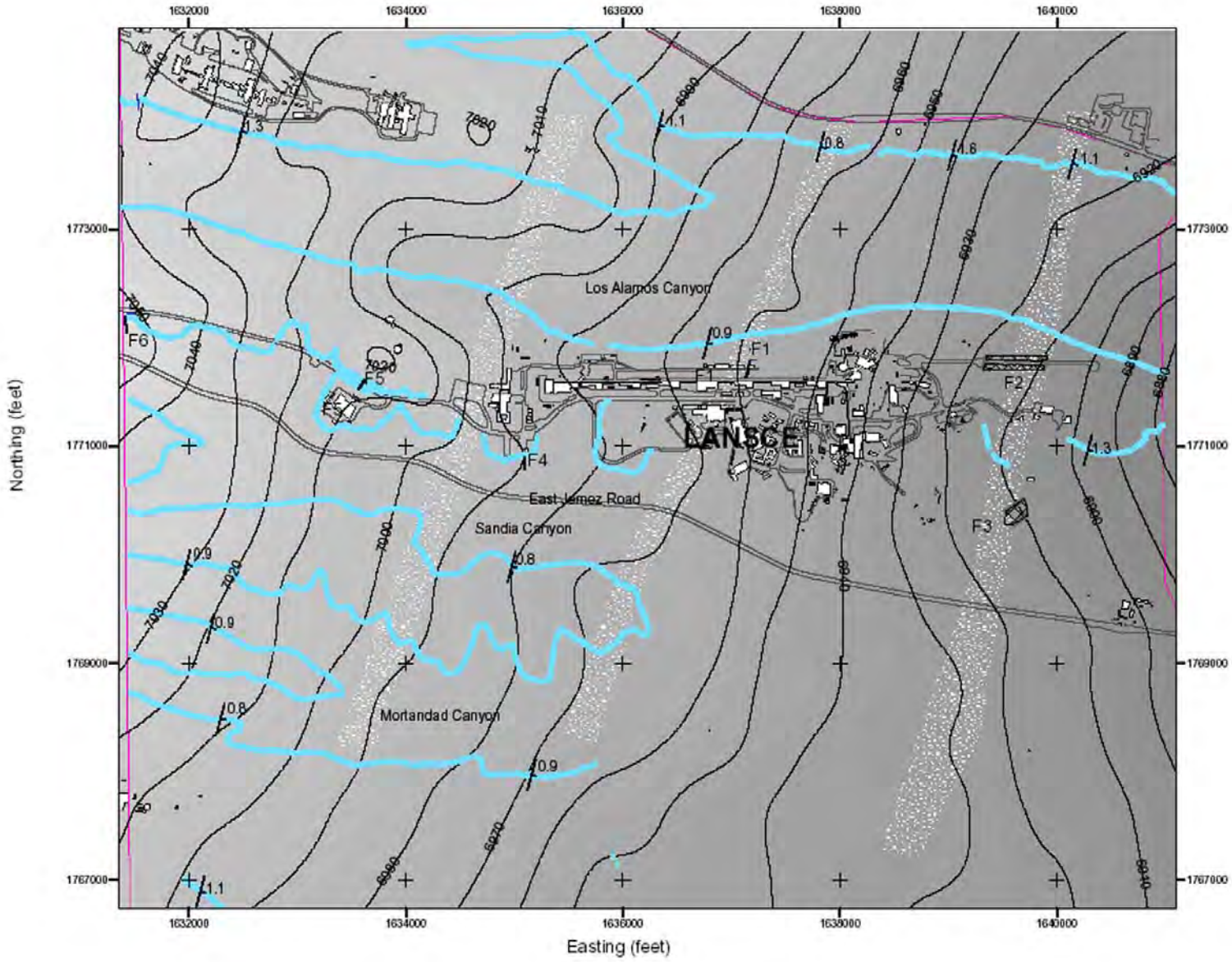

Figure 13d. Contoured upper surface of unit Qbt2. Points are derived from the mapped unit Qbt2–Qbt3 contact. Methods for generating this surface, contour interval, labeling, and uncertainties are as in Figure 13a.

where the upper part of unit Qbt1v-u and unit Qbt2 are welded together (Figure 6). The lower nonwelded portion of unit Qbt1v-u was included in unit Qbt2a of Baltz et al. (1963), in the nonwelded base of unit Qbt2 by Vaniman and Wohletz (1990) and Goff (1995), and in unit Qbt1v by Broxton and Reneau (1995) and Broxton et al. (1995a). The nonwelded to moderately welded tuffs above the welding break in unit Qbt1v-u have been included either in unit Qbt1v (Broxton and Reneau, 1995; Rogers, 1995) or in unit Qbt2 (Vaniman and Wohletz, 1990; Broxton et al., 1995a; Goff, 1995; Rogers, 1995), depending largely on the location of the study. Units Qbt2a and Qbt2b of Baltz et al. (1963) are equivalent to units Qbt1v-u and Qbt2, respectively, in the eastern part of LANL, and are combined as unit Qbt2 in the western part of LANL. Broxton and Reneau (1995) recognized that cooling units Qbt1v and Qbt2 merge to the west, and suggested that they could be combined as unit Qbt1v/2, which is equivalent to our unit Qbt2(+1vw).

Unit Qbt3 has been consistently mapped by most workers, but the lower bench-forming part of the unit was broken out as a separate nonwelded unit (Qbt-nw) by Vaniman and Wohletz (1990), Broxton et al. (1995a), and Goff (1995).

A.2 Post-Bandelier Tuff Units

Post-Bandelier Tuff units exposed in the area include older alluvium (Qoal), canyon bottom alluvium and terrace deposits (Qal+Qt), and colluvium (Qc). Although geomorphic mapping, primarily of canyon-bottom sediments in DP Canyon and portions of Los Alamos, Sandia, and Mortandad canyons (Reneau et al., 1998b; Reneau and McDonald, 1996; Katzman et al., 1999; Drakos and Reneau, unpublished mapping) shows more detail than mapping in this study, the post-Bandelier Tuff units of previous investigations generally correlate to Plate 1. Older alluvium (Qoal) was mapped in Sandia, Mortandad, and DP canyons, and on an unnamed mesa between Sandia and Mortandad canyons by Goff et al. (in prep.). We found that several of these areas are colluvium adjacent to steep outcrops of nonwelded unit Qbt3, containing abundant dacitic and andesitic clasts that have been weathered out of adjacent unit Qbt3 outcrops. These colluvial deposits differ from Qoal in that most clasts are subangular to angular, rather than rounded. Most deposits of Qoal, including those mapped in DP Canyon, contain abundant large clasts of rounded dacite, typically in a red clayey matrix. Clasts in the colluvium derived from unit Qbt3 are a mixture of andesitic and dacitic lithologies. Additionally, the colluvium displays little sign of soil development.

The nature and location of Qoal deposits in DP Canyon indicate that they were deposited during headward erosion from the Rio Grande of the tributary canyon as present day canyons were beginning to be incised, rather than just after deposition of the Bandelier Tuff, when braided streams draining off the Sierra de los Valles occupied the present mesa tops (Reneau, 1995). The upper part of this tributary to DP Canyon is plugged with older alluvium, suggesting that there has been little headward erosion in this drainage since deposition of Qoal. Nevertheless, the lower part of this canyon has been incised 3–6 m (10–20 ft) below Qoal where it is exposed along the erosional Qbt2–Qbt3 bench (Reneau, 1995). The age of Qoal in the tributary to DP Canyon and along the edge of DP mesa is not certain, but is inferred to be early Pleistocene in age based on pumice beds included in exposures of Qoal elsewhere on the Pajarito Plateau (e.g., Reneau et al., 1995; Reneau and McDonald, 1996; Gardner et al., 2001; Lewis et al., 2002; Reneau et al., 2002).

B. Structural Geology

Although several small-displacement faults were identified in the study area, our mapping reveals no major fault zones. In addition to four small-displacement faults and fault zones with clear vertical displacement on mapped contacts, we mapped a fracture and fault zone and a fault with unknown amounts of displacement. No mapped faults could be traced across mesa tops or canyons (Plate 1); trace lengths appear to be short.

Fault F1 corresponds to a fault mapped by Purtymun (1968), and lies within a zone of increased eastward dip of lower Tshirege Member units (Figures 13a–13d). Purtymun (1968) suggested 4.3 m (14 ft) of vertical displacement across this fault based on two boreholes that were located approximately 1 km (0.6 mi) apart on either side of the zone of change in dip. It is possible that the increase in dip represents an approximately 300-m-wide zone of distributed down-to-the-east deformation that could accommodate approximately 5 m (20 ft) of distributed dip-slip displacement, including fault F1; however, the increase in dip is less apparent on the top of unit Qbt2 (Figure 13d), and therefore more probably indicates deposition of underlying units on irregular topography. Fault F1 (Plate 1) also coincides approximately with the western margin of the pre-Bandelier Tuff valley (Figure 2), which may be fault-controlled, as described by Broxton and Reneau (1996).

Faults and fractures in zone F2 at the roadcut north of the lagoons in nonwelded unit Qbt3 are more abundant than fractures elsewhere in Qbt3 (including adjacent exposures), have overall greater widths, and in some cases display cataclastic textures. Many of the fractures in zones F2 and F3 may be cooling joints that were reactivated by tectonic activity (e.g., Lewis et al., 2002). Cooling joints in the Bandelier Tuff are generally vertical, evenly spaced cracks of short lateral extent and sinuous strike that commonly terminate at other joints, forming irregular polygonal columns with diameters <3 m (10 ft) (e.g., Rogers et al., 1996). The orientation of cooling joints depends on the orientation of principal stresses within the tuff during cooling; orientation of joints can be influenced by a combination of regional tectonic stresses and local stresses imposed by underlying topography during the processes of compaction and welding. Fractures in zone F2 have a mean strike direction of N12E, but comprise three prominent sets of strikes (N, N40E, and N40W). These strikes are similar to those documented in previous fracture studies in the Bandelier Tuff that show, in some localities, a crude bimodal distribution that defines a conjugate system of northwesterly and northeasterly oriented fracture sets (e.g., Purtyman et al., 1995; Wohletz, 1995, 1996, in preparation). Fracture densities in zone F2 (56 fractures/30 m) are above background fracture density and equivalent to maximum fracture densities documented in nonwelded unit Qbt3 at other sites around LANL (e.g., Kolbe et al., 1994, 1995; Purtymun et al., 1995). Locally high fracture densities are in some cases associated with known faults (Vaniman and Chipera, 1995), and have been used to infer underlying faults (Vaniman and Wohletz, 1990; Wohletz, 1995, 1996). At TA-67, however, relatively low values of fracture density have been measured near faults, and higher than average values have been measured where no faults were identified (Kolbe et al., 1994; Reneau et al., 1995). Widths of fractures and faults in zone F2 are also above background compared to other areas around LANL (e.g., Vaniman and Wohletz, 1990; Kolbe et al., 1995; Reneau et al., 1995; Vaniman and Chipera, 1995) and compared to adjacent exposures to the west on Mesita de Los Alamos.

The existence of both fracture-based and deformation band faults, as seen in fault F1 and zones F2 and F3, is not unusual in nonwelded, vapor-phase altered tuffs like unit Qbt3 (Wilson et al., 2002). Preliminary results suggest that vapor-phase alteration of a nonwelded ignimbrite increases grain-to-grain contacts within the tuff matrix, increasing its strength and allowing it to deform by fractures as well as deformation bands (Wilson et al., 2002). Individual deformation bands can be formed from as little as 1 mm to centimeters of displacement, and are well developed in faults in nonwelded tuff with <1 m (<3 ft) of displacement (Wilson et al., 2001, 2002, in prep.). Fine-grained material filling many of the fractures in zone F2 may be crushed tuff resulting from small-displacement faulting, as has been documented at MDA-G (Reneau and Vaniman, 1998). Some of the faults in zone F2 may be deformation band faults formed by grain size reduction, as determined for fault F1; however, heavy overprinting by root growth and associated deposition of clay and calcite makes it difficult to recognize fault fabrics in zone F2. The calcite in these faults likely results from biological and chemical processes in which plant roots in the faults and fractures are converted to calcite, as proposed by Newman et al. (1997) and Reneau and Vaniman (1998) for fracture fill in unit Qbt2. Without detailed structural and geochemical analysis of the material filling faults and fractures, it is not clear if the origin of fracture-filling material in zone F2 is due to infilling from the surface or cataclasis. Structures like these are the subject of ongoing study (e.g., Wilson et al., 2001, 2002, in prep.). Clay in many of the fractures is likely to be smectite-rich, as determined for other deformation band faults in nonwelded parts of unit Qbt3 (Wilson et al., 2002) and for fracture fill in welded parts of unit Qbt3 (Vaniman and Chipera, 1995; Vaniman et al., 2002). Clay may have been transported in colloidal form from the surface by water infiltrating along roots (e.g., Davenport et al., 1995; Vaniman and Chipera, 1995); however, this has not been confirmed. Wetting and drying of swelling clays like smectite likely opened cracks that acted as pathways for water.

Zones F2 and F3 coincide approximately with the eastern zone of change in dip on the top of units Qbt1g, Qbt1v-c, and Qbt1v-u. The change in dip on the top of unit Qbt2 is less apparent, suggesting that the change in dip may be due to deposition over paleotopography, but data are sparse. Based on the orientation of fractures and faults measured in zones F2 and F3 and the orientation of zone F3, it would not appear that these zones are connected; however, both zones lie along the same change in dip of Tshirege Member contacts (Figure 13a–d). We reiterate that the orientation of fractures within zone F3 is variable and may reflect the orientation of cooling joints. In addition, the orientation of fractures

in zone F2 may be biased by orientation of the exposure. We therefore cannot prove or rule out the possibility that they are connected.

Because fault F1 and zones F2 and F3 coincide with subtle changes in dip of Tshirege Member units, we entertain the possibility that the changes in dip reflect broad zones of distributed deformation. We cannot determine without more detailed mapping if these zones of change in dip are the result of distributed faulting, fault-related folding, or deposition of Tshirege Member units over irregular topography. These zones could be similar to faulted monoclines that have been mapped to the south and west in the Pajarito fault system (e.g., McCalpin, 1997; Gardner et al., 1999, 2001; Lewis et al., 2002). Such extensional fault-propagation folds have been documented to form above steeply dipping normal faults (e.g., Hardy and McClay, 1999; Withjack and Callaway, 2000; Willsey et al., 2002) and may be related to discrete normal faulting at depth, especially where a distinct mechanical contrast exists between basement and cover strata. However, decreases in changes in dip higher in the stratigraphy suggest that changes in dip may be related to deposition over paleotopography. Based on previous studies, some of the paleotopography could be fault controlled.

It is unclear if small-displacement faults mapped in this study are associated with known or inferred faults in the vicinity. Mapped faults are too far east to be part of the Pajarito, Rendija Canyon, or Guaje Mountain faults, but may be related to inferred subsurface faults (Figure 2). The Sawyer Canyon fault displaces Tshirege Member units up to 37 m down to the east near the northern end of its trace; based on fracture zones, the fault may extend south of its mapped trace (Carter and Gardner, 1995), which ends ~2.5 km north of the study area. However, if the Sawyer Canyon fault does pass through the study area, it does not offset the Tshirege Member units to any notable degree. The dispersed locations, size, and character of faults found on this part of the Pajarito Plateau suggest that they are similar to faults found to the south and east at TA-54 (Reneau et al., 1998a) and in the central part of LANL (Kolbe et al., 1994; Reneau et al., 1995). The small-displacement faults are most likely the result of diffuse adjustments associated with large earthquakes on the main Pajarito fault. In other regions during historical earthquakes, distributed subsidiary faulting has been documented up to 14 km from the main fault, especially on the downdropped block (Coppersmith and Youngs, 1992; Wells, 1993; Pezzopane and Dawson, 1996).

C. Implications for Contaminant Transport

Fault and fracture zones F2 and F3 may be significant features for subsurface transport of contaminants due to increased permeability in these zones. The abundance of roots, clay (probably at least in part transported from the surface in colloidal form), and carbonate in fault zone F2 suggest higher unsaturated permeabilities in the fractures than the host rock (Wilson et al., 2002); these fractures, therefore, may provide pathways for fluids and contaminants into the subsurface. Our identification of distributed, small-displacement faulting to the north and south of the lagoons at TA-53 raises concern that the lagoons themselves are located in a zone of distributed faulting. The lagoons (Potential Release Sites 53-002a and b) are three surface mixed-waste impoundments that have been used for treatment of liquid sanitary and radioactive waste, including tritium, from 1970 until the present. Drilling of several boreholes in this area revealed a subsurface plume of tritium contamination that extended up to 100 ft below the ground surface (LANL, 1992; Stauffer et al., 2002). It appears that some of this contamination was from discharge from an outfall structure into a drainage ditch, rather than directly from the surface impoundments. Near-surface data show the highest tritium concentrations near the intersection of the lagoons (Stauffer et al., 2002). Seven additional boreholes were drilled to better determine the extent of the subsurface tritium plume and gain a better understanding of subsurface transport of contaminants in this area (SAIC, unpublished data). A better understanding of the style and extent of deformation in this area would help to assess potential infiltration of contaminants into the subsurface. Although the identified fault and fracture zones may not pose significant seismic hazards, they are possible fast pathways for contaminants.

D. Potential for Seismic Surface Rupture and Age of Faulting

All faults mapped within the study area displace units of the 1.2-million-year-old Tshirege Member of the Bandelier Tuff, and are therefore Quaternary in age. Although some of the near-surface faults and fractures in fault zone F2 may have incorporated surficial material that is younger than the Bandelier Tuff, the age of this material is unknown. The faults mapped in this study are all small-displacement faults [<1.5 m (<5 ft) measurable on any individual fault] that likely experienced small amounts of movement during earthquakes on the Pajarito fault system.

Detailed studies elsewhere on the Pajarito Plateau have found similar small-displacement faults of the scale found in this study (e.g., Reneau et al., 1995, 1998a). The density of faults found in the study area is relatively low, with only four structures with measurable displacement on stratigraphic contacts, indicating that this is a fairly stable part of the Pajarito Plateau with relatively low potential for seismic surface rupture. Probabilistic analyses of surface rupture potential by Olig et al. (1998, 2001) at TA-3 for the Rendija Canyon fault zone and at TA-16 for the Pajarito fault suggest that even in the case of 1-in-10,000-year events, seismic surface rupture is only a measurable hazard on the main traces of the Pajarito and Rendija Canyon faults. In both cases, the main splays of the faults have cumulative vertical displacements of >15 m (>50 ft) in Tshirege Member units. Therefore, the small displacement faults found in this study have extremely low potential for seismic surface rupture. We deem it highly unlikely that these faults would be reactivated as major surface rupturing faults during future earthquakes.

VI. Conclusions

Changes in crystallization and welding characteristics of units Qbt1g through Qbt3 of the Tshirege Member of the Bandelier Tuff in the north-central to northeastern portion of LANL provided excellent stratigraphic markers for examining the structure of the area and determining the potential for seismic surface rupture. Tshirege Member units strike approximately N15E, and on average dip about 1ºE, with maximum dips of 3.4ºE. Lateral variations in welding in units Qbt1v and Qbt2 led us to modify stratigraphic nomenclature of parts of these units, which helps clarify inconsistencies in previous mapping of the unit Qbt1v–Qbt2 contact. Our investigations revealed several small-displacement faults with limited lateral extent. No individual fault had >1.5 m (>5 ft) of vertical (primarily down-to-the-west) displacement of mapped contacts; however, several faults and fractures crop out in areas where no stratigraphic markers were exposed to determine the amount of displacement. The presence of faulting in these areas was based on identification of cataclastic textures including deformation bands, which are typical of faults in nonwelded tuffs and unlithified sediments. The zone of fractures and faults exposed to the north of the TA-53 lagoons additionally has fracture densities and widths above background levels for this area and other areas of the Pajarito Plateau. Some faults and fracture zones coincide with changes in dip (on the order of 1º–2º) of mapped Tshirege Member contacts. Changes in dip could reflect distributed faulting, but more likely reflect deposition of units on irregular topography, which is supported by smaller changes in dip higher in the stratigraphic section. Faulting in the area occurred some time since 1.2 Ma, based on displacement on the Tshirege Member of the Bandelier Tuff. Mapped faults and fracture zones lie east of the Pajarito fault system and are not clearly connected with the Sawyer Canyon fault or other mapped or inferred structures. Rather, these small-displacement faults likely represent subsidiary distributed faulting associated with earthquakes on the Pajarito fault system. The distribution and size of faults found in this study suggest that the area is a relatively stable part of the Pajarito Plateau with extremely low potential for seismic surface rupture.

VII. Acknowledgements

This work was supported by the LANL Seismic Hazards Program under the direction of Larry Goen and by planning efforts for a proposed Advanced Hydrotest Facility. We thank Carolyn Zerkle, Jim Holt, and the Office of Infrastructure, Facilities, and Construction of the LANL Operations Directorate for support. We also thank Phil Noll and the Advanced Hydrotest Facility (AHF) program office for initial support of the project. Dave Broxton and Dave Vaniman provided helpful discussions and insights on issues regarding the stratigraphy of the Bandelier Tuff. We thank Emily Kluk and Steve Chipera for XRF and XRD analyses, respectively, LANL's Geographic Information System Laboratory for invaluable assistance with cartography and database management, Anthony Garcia for graphic design, and Steve Reneau for a helpful review.

References

Bailey, R. A., R. L. Smith, and C. S. Ross. 1969. Stratigraphic nomenclature of volcanic rocks in the Jemez Mountains, New Mexico, U. S. Geological Survey Bulletin 1274-P, 19 pp.

Baldridge, W. S., P. W. Dickerson, R. E. Riecker, and J. Zidek, Eds. 1984. *Rio Grande Rift: Northern New Mexico*, New Mexico Geological Society Guidebook 35, 379 pp.

Baldridge, W. S., G. R. Keller, V. Haak, E. Wendlandt, G. R. Jiracek, and K. H. Olsen. 1995. The Rio Grande rift, in *Continental Rifts: Evolution, Structure, Tectonics*. K. H. Olsen, Ed. (Elsevier, Amsterdam, Holland), pp. 233–275.

Baltz, E. H., J. H. Abrahams, Sr., W. D. Purtymun. 1963. Preliminary report of geology and hydrology of Mortandad Canyon near Los Alamos, New Mexico, with reference to disposal of liquid low-level radioactive wastes, U. S. Geological Survey open-file report, Albuquerque, New Mexico, 105 pp.

Broxton, D. E., and S. L. Reneau. 1995. Stratigraphic nomenclature of the Bandelier Tuff for the Environmental Restoration project at Los Alamos National Laboratory, Los Alamos National Laboratory report LA-13010-MS, 21 pp.

Broxton, D. E., and S. L. Reneau. 1996. Buried early Pleistocene landscapes beneath the Pajarito Plateau, northern New Mexico, in New Mexico Geological Society Guidebook 47, pp. 325–345.

Broxton, D. E., G. H. Heiken, S. J. Chipera, and F. M. Byers, Jr. 1995a. Stratigraphy, petrography, and mineralogy of the Bandelier Tuff and Cerro Toledo deposits, in Earth science investigations for environmental restoration—Los Alamos National Laboratory Technical Area 21, D. E. Broxton and P. G. Eller, Eds., Los Alamos National Laboratory report LA-12934-MS, pp. 33–63.

Broxton, D. E., P. A. Longmire, P. G. Eller, and D. Flores. 1995b. Preliminary drilling results for boreholes LADP-3 and LADP-4, in Earth science investigations for environmental restoration—Los Alamos National Laboratory Technical Area 21, D. E. Broxton and P. G. Eller, Eds. Los Alamos National Laboratory report LA-12934-MS, pp. 93–109.

Budding, A. J. 1978. Gravity survey of the Pajarito Plateau, Los Alamos and Santa Fe Counties, New Mexico, Los Alamos National Laboratory report LA-7419-MS, 15 pp.

Carey, W. J., and G. Cole. 2002. Description of the Cerro Grande fire laser altimetry (LIDAR) data set, Los Alamos National Laboratory report LA-13892-MS, 56 pp.

Carter, K. E., and J. N. Gardner. 1995. Quaternary fault kinematics in the northwestern Española basin, Rio Grande rift, New Mexico, in New Mexico Geological Society Guidebook 46, pp. 97–103.

Cas, R. A. F., and J. V. Wright. 1987. *Volcanic Successions, Modern and Ancient* (Allen and Unwin Publishers, London), pp. 1–528.

Chipera, S. J. and D. L. Bish. 2002. FULLPAT: A full pattern quantitative analysis program for x-ray powder diffraction using measured and calculated patterns, *J. Appl. Cryst.* **35**, pp. 744–749.

Cole, G., W. J. Carey, D. Vaniman, and D. E. Broxton. In preparation. Development of the FY02 3-dimensional geologic model of the Los Alamos National Laboratory and surrounding area.

Coppersmith, K. J., and R. R. Youngs. 1992. Modeling fault-rupture hazard for the proposed repository and Yucca Mountain, Nevada, in *High-Level Radioactive Waste Management, Proceedings of the Third International Conference, Las Vegas, Nevada*, Vol. 1, pp. 142–1150.

Crowe, B., G. Linn, G. Heiken, and M. Bevier. 1978. Stratigraphy of the Bandelier Tuff in the Pajarito Plateau, applications to waste management, Los Alamos National Laboratory report LA-7225-MS, 57 pp.

Davenport., D. W., B. P. Wilcox, and B. L. Allen. 1995. Micromorphology of pedogenically derived fracture fills in Bandelier Tuff, New Mexico, *Soil Sci. Soc. Am. J.* **59** (6), pp. 1672–1683.

Deutsch, C. V., and A. G. Journel. 1992. *GSLIB Geostatisical Software Library and Users Guide* (Oxford University Press, New York).

Dransfield, B. J., and J. N. Gardner. 1985. Subsurface geology of the Pajarito Plateau, Española basin, New Mexico, Los Alamos National Laboratory report LA-10455-MS, 15 pp.

Fergusson, J. F., W. S. Baldridge, L. W. Braile, S. Biehler, B. Gilpin, and G. R. Jiracek. 1995. Structure of the Española basin, Rio Grande rift, New Mexico, from SAGE seismic and gravity data, in New Mexico Geological Society Guidebook 46, pp. 105–110.

Gardner, J. N., and F. Goff. 1984. Potassium-argon dates from the Jemez volcanic field: Implications for tectonic activity in the north-central Rio Grande rift, in New Mexico Geological Society Guidebook 35, pp. 75–81.

Garner, J. N., and L. House. 1987. Seismic hazards investigations at Los Alamos National Laboratory, 1984 to 1985, Los Alamos National Laboratory report LA-11072, 76 pp.

Gardner, J. N., and L. House. 1994. Surprisingly high intensities from two small earthquakes, northern Rio Grande rift, New Mexico, *EOS, Trans. Amer. Geophys. U.* **75** (16), p. 128.

Gardner, J. N., and L. S. House. 1999. High modified mercalli intensities from small shallow earthquakes, northern Rio Grande rift, New Mexico, USA, *EOS, Trans. Amer. Geophys. U.* **80** (46), p. F710.

Gardner, J. N., F. Goff, S. Garcia, and R. C. Hagan. 1986. Stratigraphic relations and lithologic variations in the Jemez volcanic field, New Mexico, *J. Geophys. Res.* **91** (B2), pp. 1763–1778.

Gardner, J. N., W. S. Baldridge, R. Gribble, K. Manley, K. Tanaka, J. W. Geissman, M. Gonzalez, and G. Baron. 1990. Results from seismic hazards trench #1 (SHT-1), Los Alamos seismic hazards investigations, Los Alamos National Laboratory unpublished report EES1-SH90-19.

Gardner, J. N., A. Lavine, D. Vaniman, and G. WoldeGabriel. 1998. High-precision geologic mapping to evaluate the potential for seismic surface rupture at TA-55, Los Alamos National Laboratory, Los Alamos National Laboratory report LA-13456-MS, 13 pp.

Gardner, J. N., A. Lavine, G. WoldeGabriel, D. Krier, D. Vaniman, F. Caporuscio, C. Lewis, P. Reneau, E. Kluk, and M. J. Snow. 1999. Structural geology of the northwestern portion of Los Alamos National Laboratory, Rio Grande rift, New Mexico: Implications for seismic surface rupture potential from TA-3 to TA-55, Los Alamos National Laboratory report LA-13589-MS, 112 pp.

Gardner, J. N., S. L. Reneau, C. J. Lewis, A. Lavine, D. Krier, G. WoldeGabriel, and G. Guthrie. 2001. Geology of the Pajarito fault zone in the vicinity of S-Site (TA-16), Los Alamos National Laboratory, Rio Grande rift, New Mexico, Los Alamos National Laboratory report LA-13831-MS, 86 pp.

Gardner, J. N., S. L. Reneau, A. Lavine, C. J. Lewis, D. Katzman, E. V. McDonald, J. Wilson, L. Goodwin, K. I. Kelson, K. Lepper, and C. Wilson. In preparation. Paleoseismic trenching in the Guaje Mountain fault zone, Pajarito fault system, Rio Grande rift, New Mexico, Los Alamos National Laboratory report.

Goff, F. 1995. Geologic map of Technical Area 21 in Earth science investigations for environmental restoration—Los Alamos National Laboratory Technical Area 21 D. E. Broxton and P. G. Eller, Eds., Los Alamos National Laboratory report LA-12934-MS, pp. 7–18.

Goff, F., J. N. Gardner, and S. L. Reneau. In preparation. Geologic map and structure of the Frijoles quadrangle, Los Alamos, and Sandoval Counties, New Mexico, New Mexico Bureau of Mines and Mineral Resources geologic quadrangle map, Los Alamos National Laboratory document LA-UR-016657.

Hardy, S., and K. McClay. 1999. Kinematic modelling of extensional fault-propagation folding, *J. Struc. Geol.* **21** (7), pp. 695–702.

Izett, G. A., and J. D. Obradovich. 1994. $^{40}Ar/^{39}Ar$ age constraints for the Jaramillo normal subchron and the Matuyama-Brunhes geomagnetic boundary, *J. Geophys. Res.* **99** (B2), pp. 2925–2934.

Katzman, D., R. Ryti, M. Tardiff, and B. Hardesty. 1999. Evaluation of sediment and alluvial groundwater in DP Canyon: Reaches DP-1, DP-2, DP-3, and DP-4, Los Alamos National Laboratory document LA-UR-99-4238.

Keller, G. R., Ed. 1986. Special section on the Rio Grande rift, *J. Geophys. Res.* **91** (B6), pp. 6142–6345.

Kelley, V. C. 1979. Tectonics, middle Rio Grade rift, New Mexico, in *Rio Grande Rift: Tectonics and Magmatism*, R. E. Riecker, Ed. (American Geophysical Union, Washington, D. C.), pp. 57–70.

Kelson, K. I., and S. S. Olig. 1995. Estimated rates of Quaternary crustal extension in the Rio Grande rift, northern New Mexico, in New Mexico Geological Society Guidebook 46, pp. 9–12.

Kelson, K. I., M. A. Hemphill-Haley, S. S. Olig, G. D. Simpson, J. N. Gardner, S. L. Reneau, T. R. Kolbe, S. L. Forman, and I. G. Wong. 1996. Late-Pleistocene and possibly Holocene displacement along the Rendija Canyon fault, Los Alamos County, New Mexico in New Mexico Geological Society Guidebook 47, pp. 153–160.

Kolbe, T., J. Sawyer, A. Gorton, S. Olig, D. Simpson, C. Fenton, S. Reneau, J. Carney, J. Bott, and I. Wong. 1994. Evaluation of the potential for surface faulting at the proposed Mixed Waste Disposal Facility, TA-67. Unpublished consulting report prepared for Los Alamos National Laboratory by Woodward-Clyde Federal Services, Oakland, CA, 3 Vols.

Kolbe, T., J. Sawyer, J. Springer, S. Olig, S. Reneau, M. Hemphill-Haley, and I. Wong. 1995. Evaluation of the potential for surface faulting at TA-63. Unpublished consulting report prepared for Los Alamos National Laboratory by Woodward-Clyde Federal Services, Oakland, CA.

Kuhn, A. In preparation. Report of pre-conceptual geotechnical investigations, Advanced Hydrotest Facility project, TA-53, Los Alamos National Laboratory, Los Alamos, New Mexico, Project No. C59010120. Unpublished consulting report submitted by Kleinfelder, Inc., to C. Robert Hutchins, Project Manager, Holmes & Narver/ Raytheon.

Lewis, C. J., A. Lavine, S. L. Reneau, J. N. Gardner, R. Channell, and W. Criswell. 2002. Geology of the western part of Los Alamos National Laboratory (TA-3 to TA-16), Rio Grande rift, New Mexico, Los Alamos National Laboratory report LA-13960-MS, 98 pp.

LANL (Los Alamos National Laboratory. 1992. RCRA Part B Permit Application, Surface Impoundments, Technical Area 53, Revision 1, Los Alamos National Laboratory, Environmental Protection group, EM-8, Los Alamos, New Mexico.

Machette, M. N., S. F. Personius, K. I. Kelson, K. M. Haller, and R. L Dart. 1998. Map and data for Quaternary faults and folds in New Mexico, (1 plate, scale 1:750,000), U. S. Geological Survey, open-file report 98-521, 443 pp.

Manley, K. 1979. Stratigraphy and structure of the Española basin, Rio Grande rift, New Mexico, in *Rio Grande Rift: Tectonics and Magmatism*, R. E. Riecker, Ed. (American Geophysical Union, Washington, D. C.), pp. 71–86.

McCalpin, J. P. 1997. Geomorphology and structure of the Pajarito fault zone west of Los Alamos National Laboratory, New Mexico. Unpublished consulting report prepared for Los Alamos National Laboratory by GEO-HAZ Consulting, Inc., Estes Park, CO.

McCalpin, J. P. 1998. Late Quarternary faulting on the Pajarito fault, west of Los Alamos National Laboratory, north-central New Mexico: Results from the seven-trench transect excavated in summer of 1997. Unpublished consulting report prepared for Los Alamos National Laboratory by GEO-HAZ Consulting, Inc., Estes Park, CO.

McCalpin, J. P. 1999. Late Quaternary faulting on the Pajarito fault, west of Los Alamos National Laboratory, north-central New Mexico: Results from seven trenches excavated in summer 1998. Unpublished consulting report prepared for Los Alamos National Laboratory by GEO-HAZ Consulting, Inc., Estes Park, CO.

McDonald, E. V., S. L. Reneau, and J. N. Gardner. 1996. Soil-forming processes on the Pajarito Plateau: Investigation of a soil chronosequence in Rendija Canyon, in New Mexico Geological Society Guidebook 47, pp. 367–374.

Newman, B. D., A. R. Campbell, D. I. Norman, and D. B. Ringelberg. 1997. A model for microbially induced precipitation of vadose-zone calcites in fractures at Los Alamos, New Mexico, USA, *Geochim. Cosmochim. Acta* **61** (9), pp. 1783–1792.

Olig, S. S., K. I. Kelson, J. N. Gardner, S. L. Reneau, and M. Hemphill-Haley. 1996. The earthquake potential of the Pajarito fault system, New Mexico, in New Mexico Geological Society Guidebook 47, pp. 143–151.

Olig, S., R. Youngs, and I. Wong. 1998. Probabilistic seismic hazard analysis for surface fault displacement at TA-3, Los Alamos National Laboratory. Unpublished consulting report prepared for Los Alamos National Laboratory by Woodward-Clyde Federal Services, Oakland, CA.

Olig, S., R. Youngs, and I. Wong. 2001. Probabilistic seismic hazard analysis for the surface fault displacement at TA-16, Los Alamos National Laboratory. Unpublished report prepared for Los Alamos National Laboratory by URS, Inc., Oakland, CA.

Pezzopane, S. K. and T. E. Dawson. 1996. Fault displacement hazard: A summary of issues and information, in Seismotectonic framework and characterization of faulting at Yucca Mountain, Nevada, J. W. Whitney, Coordinator., U. S. Geological Survey.

Purtymun, W. D. 1968. Near-surface rocks, in Geologic studies and material properties investigations of Mesita de Los Alamos, D. Keller, Comp., Los Alamos National Laboratory report, LA-3728, pp. 9–17.

Purtymun, W. D. 1995. Geologic and hydrologic records of observation wells, test holes, test wells, supply wells, springs, and surface water stations in the Los Alamos area, Los Alamos National Laboratory report LA-12883-MS, 339 pp.

Purtymun, W. D., E. Koenig, T. Morgan, and E. Sagan. 1995. Joint orientation and characteristics as observed in a trench excavated near TA-3 and a basement excavated at TA-55, Los Alamos National Laboratory report LA-13036-MS, 42 pp.

Reneau, S. L. 1995. Geomorphic studies at DP Mesa and vicinity, in Earth science investigations for environmental restoration—Los Alamos National Laboratory Technical Area 21, D. E. Broxton and P. G. Eller, Eds., Los Alamos National Laboratory report LA-12934-MS, pp. 65–92.

Reneau, S. L. 2000. Stream incision and terrace development in Frijoles Canyon, Bandelier National Monument, New Mexico, and the influence of lithology and climate, *Geomorphology* **32**, pp. 171–193.

Reneau, S. L., and E. V. McDonald. 1996. Landscape history and processes on the Pajarito Plateau, northern New Mexico, Rocky Mountain Cell, Friends of the Pleistocene Field Trip Guidebook, Los Alamos National Laboratory document LA-UR-96-3035, 195 pp.

Reneau, S. L., and D. T. Vaniman. 1998. Fracture characteristics in a disposal pit on Mesita del Buey, Los Alamos National Laboratory, Los Alamos National Laboratory report LA-13539-MS, 21 pp.

Reneau, S. L., T. R. Kolbe, D. T. Simpson, J. S. Carney, J. N. Gardner, S. S. Olig, and D. T. Vaniman. 1995. Surficial materials and structure at Pajarito Mesa, in Geological site characterization for the proposed Mixed Waste Disposal Facility, Los Alamos National Laboratory, S. L. Reneau and R. Raymond, Eds., Los Alamos National Laboratory report LA-13089-MS, pp. 31–69.

Reneau, S. L., E. V. McDonald, J. N. Gardner, R. T. Kolbe, J. S. Carney, P. M. Watt, and P A. Longmire. 1996a. Erosion and deposition on the Pajarito Plateau, New Mexico, and implications for geomorphic responses to late Quaternary climate changes, in New Mexico Geological Society Guidebook 47, pp. 391–397.

Reneau, S. L., J. N. Gardner, and S. L. Forman. 1996b. New evidence for the age of the youngest eruptions in the Valles caldera, New Mexico, *Geology* **24**, pp. 7–10.

Reneau, S. L., D. E. Broxton, J. S. Carney, and C. LaDelfe. 1998a. Structure of the Tshirege Member of the Bandelier Tuff at Mesita del Buey, Technical Area 54, Los Alamos National Laboratory, Los Alamos National Laboratory report LA-13538-MS, 16 pp.

Reneau, S. L., R. Ryti, M. Tardiff, and J. Linn. 1998b. Evaluation of sediment contamination in upper Los Alamos Canyon: Reaches LA-1, LA-2, and LA-3, Los Alamos National Laboratory document LA-UR-98-3974.

Reneau, S. L., J. N. Gardner, A. Lavine, E. V. McDonald, C. Lewis, D. Katzman, G. WoldeGabriel, D. Krier, D. Bergfeld, and J. Heikoop. 2002. Paleoseismic investigation of trench EOC-2, Pajarito fault zone, Los Alamos National Laboratory, New Mexico, Los Alamos National Laboratory report LA-13939-MS, 65 pp.

Riecker, R. E., Ed. 1979. *Rio Grande Rift: Tectonics and Magmatism*. (American Geophysical Union, Washington, D. C.), 438 pp.

Rogers, M. A. 1995. *Geologic Map of Los Alamos National Laboratory Reservation*, (scale 1:400), State of New Mexico Environment Department, Santa Fe, NM.

Rogers, M. A., K. E. Budding, and C. V. L. Christie. 1996. Distinguishing tectonic joints from cooling joints in the Bandelier Tuff (Pleistocene), Pajarito Plateau, Los Alamos County, New Mexico, New Mexico Geological Society Guidebook 47, pp. 293–301.

Sandford, A. R., L. H. Jaksha, and D. J. Cash. 1991. Seismicity in the Rio Grande rift, in *Neotectonics of North America, Decade Map*, Vol. 1, D. B. Slemmons, E. R. Engdahl, E. M. D. Zobeck, and D. D. Blackwell, Eds. (Geological Society of America, Boulder, CO), pp. 229–244.

Schlinger, C. M., J. G. Rosenblum, and D. R. Veblen. 1988. Fe-oxide microcrystals in in welded tuff from southern Nevada: Origin of remanence carriers by precipitation in volcanic glass, *Geology* **1**, pp. 556–559.

Smith, R. L., and R. A. Bailey. 1966. The Bandelier Tuff: A study of ash-flow eruption cycles from zoned magma chambers, *Bull. Volcan.* **29**, pp. 83–104.

Smith, R. L., R. A. Bailey, and C. S. Ross. 1970. Geologic map of the Jemez Mountains, New Mexico, (map I-571, scale 1:125,000), U. S. Geological Survey investigations.

Stauffer, P., G. Escobedo-Lopez, and R. Budd. 2002. Tritium transport beneath surface impoundments at TA-53, modeling and analysis in support of data needs, Los Alamos National Laboratory document LA-UR-02-5321.

Steck, L. K., C. H. Thurber, M. C. Fehler, W. J. Lutter, P. M. Roberts, W. S. Baldridge, D. G. Stafford, and R. Sessions. 1998. Crust and upper mantle P-wave velocity structure beneath Valles caldera, New Mexico: Results from the Jemez teleseismic tomography experiment, *J. Geophys. Res.* **103** (B10), pp. 24,301–24,320.

Stimac, J., D. Hickmott, R. Abell, A. C. L. Larocque, D. Broxton, J. Gardner, S. Chipera, J. Wolff, and E. Gauerke. 1996. Redistribution of Pb and other volatile trace metals during eruption, devitrification, and vapor-phase crystallization of the Bandelier Tuff, New Mexico, *J. Volcan. Geotherm. Res.* **73**, pp. 245–266.

Toyoda, S., F. Goff, S. Ikeda, and M. Ikeya. 1995. ESR dating of quartz phenocrysts in the El Cajete and Battleship Rock Members of the Valles rhyolite, Valles caldera, New Mexico, *J. Volcan. Geotherm. Res.* **67**, pp. 29–40.

Vaniman, D., and S. Chipera. 1995. Mesa-penetrating fractures, fracture mineralogy, and fault traces at Pajarito Mesa, in Geological site characterization for the proposed Mixed Waste Disposal Facility, S. L. Reneau and R. Raymond, Jr., Eds., Los Alamos National Laboratory report LA-13089-MS, pp. 71–85.

Vaniman, D., and K. Wohletz. 1990. Results of geological mapping/fracture studies: TA-55 area, Los Alamos National Laboratory Seismic Hazards program memorandum EES1-SH90-17, (3 plates, 23 figures), 25 pp.

Vaniman, D., S. Chipera, D. L. Bish, M. C. Duff, and D. B. Hunter. 2002. Crystal chemistry of clay-Mn oxide associations in soils, fractures, and matrix of the Bandelier Tuff, Pajarito Mesa, New Mexico, *Geochim Cosmochim Acta* **66** (8), pp. 1349–1374.

Vaniman, D., G. Cole, and D. Broxton. In preparation. From drill-hole data to 3-D geologic models, in Groundwater Annual Status Report—2001, C. Nylander, Ed., Los Alamos National Laboratory report.

Wells, D. L. 1993. Analysis of primary and secondary surface faulting associated with historical normal and strike-slip earthquakes, *Geo. Soc. Am. Abs. Prog.* **25** (5), p. 161.

Williston, McNeil, and Associates. 1979. A time domain survey of the Los Alamos region, New Mexico, Los Alamos Scientific Laboratory report LA-7657-MS, 32 pp.

Willsey, S. P., P. J. Umhoefer, and G. E. Hilley. 2002. Early evolution of an extensional monocline by a propagating normal fault: 3D analysis from combined field study and numerical modeling, *J. Struc. Geo.* **24** (4), pp. 651–669.

Wilson, J. E., L. B. Goodwin, and C. J. Lewis. 2001. Petrophysical controls on fault-zone deformation on ash-flow tuffs—Deformation bands versus fractures and implications for fluid-fault interaction, *EOS, Trans. Am. Geophys. U.* **82**, p. F1191.

Wilson, J. E., L. B. Goodwin, and C. J. Lewis. 2002. Petrophysical controls on deformation and fluid-fault interaction in the ignimbrite sequences at Los Alamos, NM, and Busted Butte, NY, *EOS, Trans Am. Geophys. U.* **83** (47), Fall Meeting supplement, Abstract T21A-1070.

Wilson, J. E., L. B. Goodwin, and C. J. Lewis, In preparation. Deformation bands in non-welded ignimbrites: Perophysical controls on fault-zone deformation and implications for fluid flow, *Geology.*

Withjack, M. O., and S. Callaway. 2000. Active normal faulting beneath a salt layer: An experimental study of deformation patterns in the cover sequence, *Am. Assoc. Pet. Geo. Bull.* **84** (5), pp. 627–651.

Wohletz, K. H. 1995. Measurement and analysis of rock fractures in the Tshirege Member of the Bandelier Tuff along Los Alamos Canyon adjacent to Technical Area 21, in Earth science investigations for environmental restoration—Los Alamos National Laboratory Technical Area 21, D. E. Broxton and P. G. Eller, Eds., Los Alamos National Laboratory report LA-12934-MS, pp. 19–32.

Wohletz, K. H. 1996. Fracture characterization of the Bandelier Tuff in OU-1098 (TA-2 and TA-41), Los Alamos National Laboratory report LA-13194-MS, 19 pp.

Wohletz, K. H. In preparation. Fractures in welded tuff, in The Tuff Handbook, G. Heiken and D. E. Broxon, Eds., Geological Society of America special paper, Los Alamos National Laboratory document LA-UR-99-6556.

Wolff, J. A., and J. N. Gardner. 1995. Is the Valles caldera entering a new cycle of activity? *Geology* **23**, pp. 411–414.

Wong, I., K. Kelson, and M. Hemphill-Haley. 1991. Evaluation of the potential for surface rupture. Unpublished consulting report prepared for Los Alamos National Laboratory by Woodward-Clyde Consultants, Oakland, CA.

Wong, I., K. Kelson, S. Olig, T. Kolbe, M. Hamphill-Haley, J. Bott, R. Green, H. Kanakari, J. Sawyer, W. Silva, C. Stark, C. Haraden, C. Fenton, J. Unruh, J. Gardner, S. Reneau, and L. House. 1995. Seismic hazards evaluation of the Los Alamos National Laboratory, 3 Vols. Unpublished consulting report prepared for Los Alamos National Laboratory by Woodward-Clyde Federal Services, Oakland, CA.

Wong, I., K. Kelson, S. Olig, J. Bott, R. Green, T. Kolbe, M. Hemphill-Haley, J. Gardner, S. Reneau, and W. Silva. 1996. Earthquake potential and ground shaking hazard at the Los Alamos National Laboratory, New Mexico, in New Mexico Geological Society guidebook, 47th Jemez Mountains Region Field Conference edition, pp. 135–142.

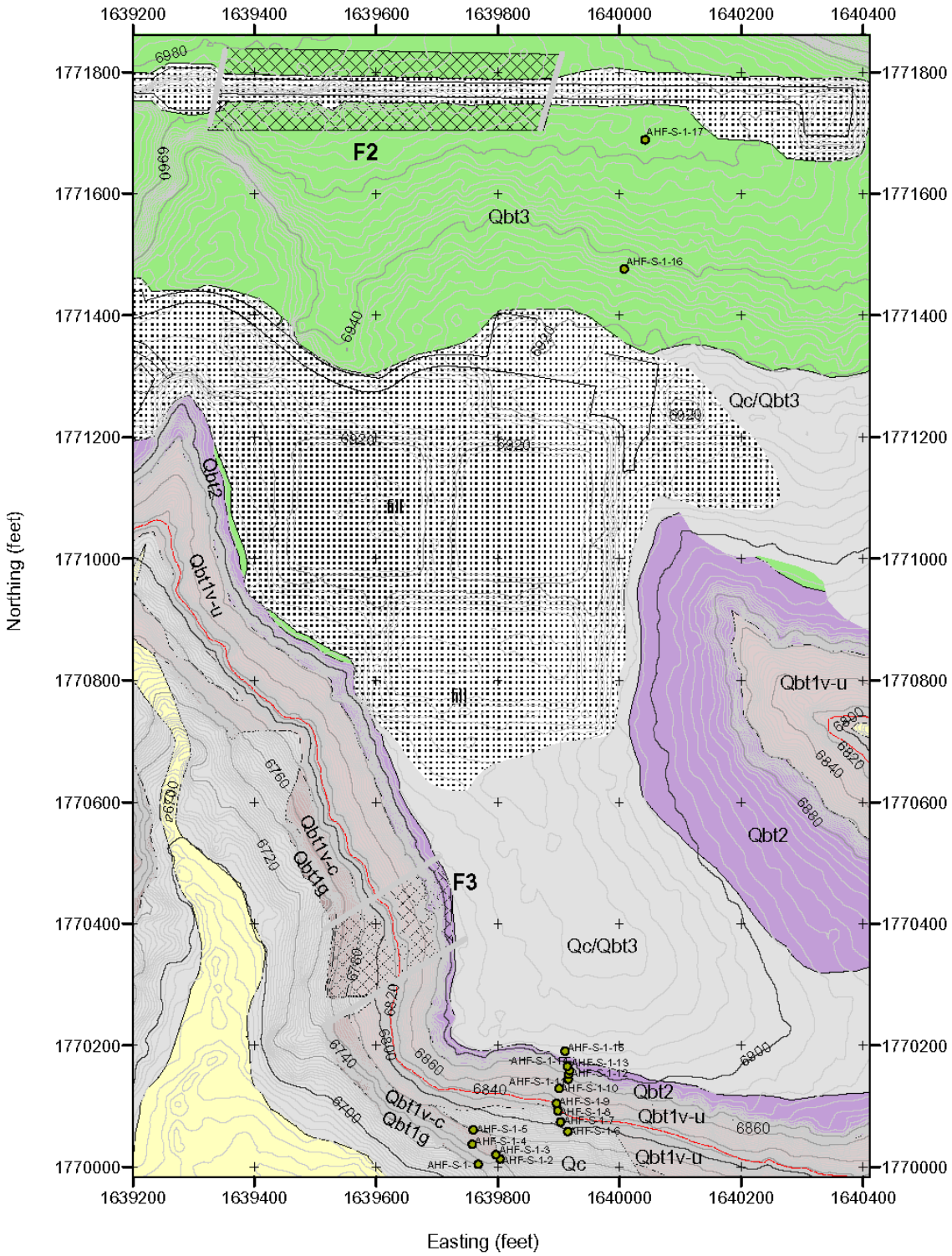

Figure A-1. Geologic map showing the location of samples from stratigraphic section AHF-S-1. The contour interval is 2 ft and is derived from the 4-ft grid, 2000 LIDAR DEM (Carey and Cole, 2002). Map units and symbols are as on Plate 1. The grid is in the State Plane Coordinate System, New Mexico Central Zone, 1983 North American Datum (in feet).

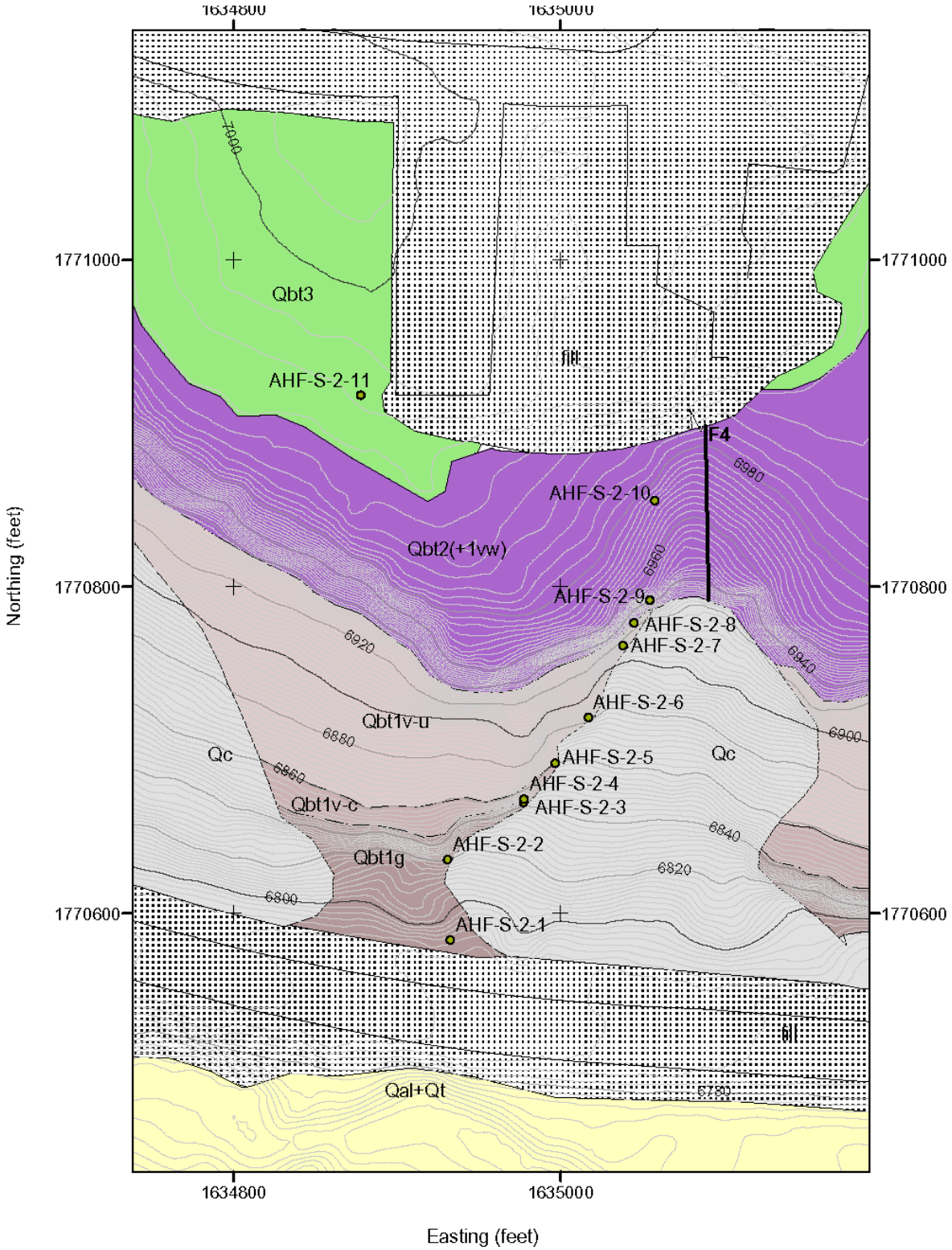

Figure A-2. Geologic map showing the location of samples from stratigraphic section AHF-S-2. The contour interval and grid are as in Figure A-1. Map units and symbols are as on Plate 1.

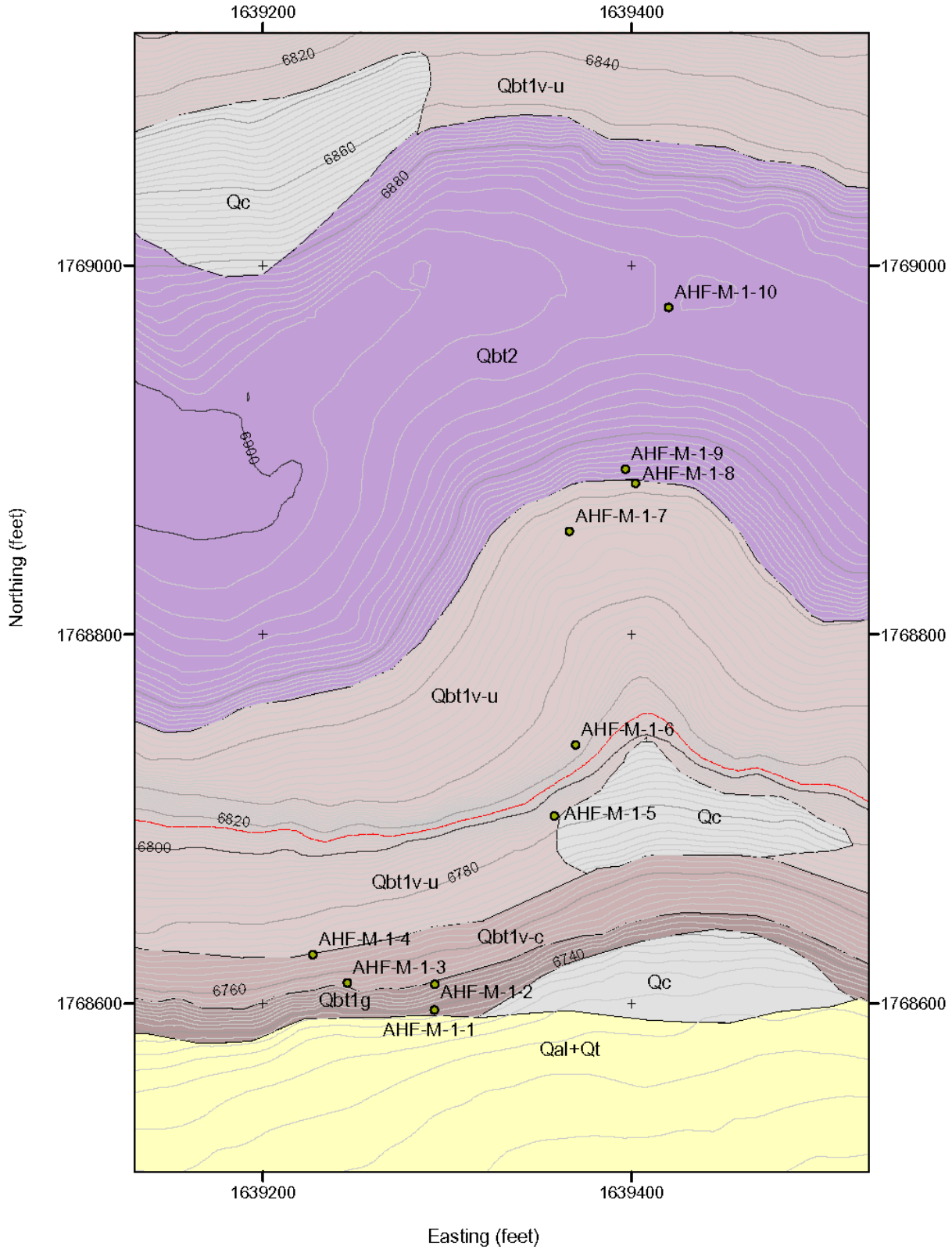

Figure A-3. Geologic map showing the location of samples from stratigraphic section AHF-M-1. The cntour interval and grid are as in Figure A-1. Map units and symbols are as on Plate 1.

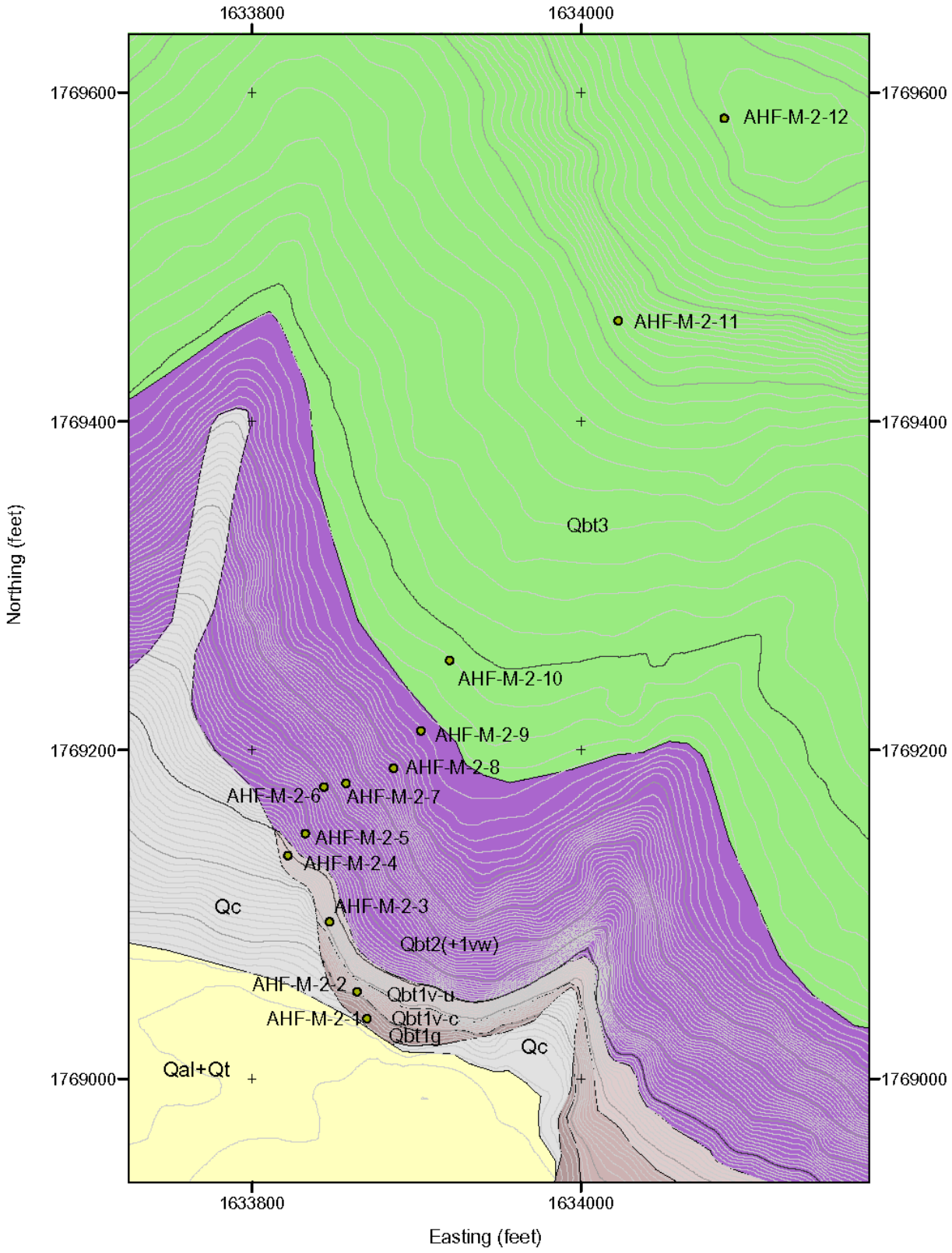

Figure A-4. Geologic map showing the location of samples from stratigraphic section AHF-M-2. The contour interval and grid are as in Figure A-1. Map units and symbols are as on Plate 1.

Appendix B. Mineralogy of Samples from Whole-Rock X-Ray Diffraction Analyses

Sample	Tridymite	Cristobalite	Opal-CT	Quartz	K-spar	Plagioclase	Glass	Hematite	Mica	Hornblende	Other	Other wt%	Total
AHF-S-1-1	0.7	0.0	0.0	12.3	6.4	12.9	69.6	0.0	0.0	0.0	---	---	102.0
AHF-S-1-2	0.7	0.0	0.0	15.5	8.6	15.4	62.4	0.0	0.0	0.0	---	---	102.7
AHF-S-1-3	1.0	0.1	0.0	15.0	9.8	18.4	58.6	0.4	0.0	0.0	---	---	103.3
AHF-S-1-4	13.8	7.1	0.0	16.4	24.8	32.9	5.0	1.3	0.0	0.0	Scapolite	1.8	103.1
AHF-S-1-5	0.6	13.9	0.0	19.2	25.3	40.5	0.0	1.1	0.0	0.1	Scapolite	1.2	101.9
AHF-S-1-6	16.6	3.0	0.0	13.3	27.2	35.0	0.0	0.5	0.0	0.1	Scapolite	1.6	97.2
AHF-S-1-7	20.6	0.2	0.0	19.3	25.6	32.6	0.0	0.8	0.0	0.0	Scapolite	0.7	99.9
AHF-S-1-8	25.3	0.0	0.0	13.1	25.5	32.0	0.0	0.9	0.0	0.1	---	---	96.9
AHF-S-1-9	22.8	0.0	0.0	12.9	26.2	37.8	0.0	0.9	0.0	0.1	---	---	100.6
AHF-S-1-10	23.3	0.0	0.0	15.0	25.0	37.1	0.0	0.8	0.0	0.0	---	---	101.2
AHF-S-1-11	23.7	0.0	0.0	15.9	24.6	37.9	0.0	0.7	0.0	0.0	---	---	102.7
AHF-S-1-12	22.4	0.0	0.0	14.9	26.0	36.6	0.0	1.1	0.0	0.0	---	---	100.9
AHF-S-1-13	24.4	0.0	0.0	15.9	24.7	33.9	0.0	1.0	0.0	0.0	---	---	99.9
AHF-S-1-14	22.0	0.0	0.0	15.2	24.5	39.7	0.0	0.7	0.0	0.0	---	---	102.2
AHF-S-1-15	23.3	1.3	0.0	14.3	24.7	35.9	0.0	1.5	0.0	0.0	---	---	101.1
AHF-S-1-16	14.4	3.5	0.0	17.9	27.8	35.6	0.0	1.0	0.0	0.0	---	---	100.3
AHF-S-1-17	10.6	5.6	0.0	17.1	28.8	38.1	0.0	0.8	0.0	0.0	---	---	101.0
									0.0				
AHF-S-2-1	1.1	0.0	0.0	11.4	8.5	19.6	60.1	0.0	0.0	0.0	---	---	100.8
AHF-S-2-2	1.0	0.0	0.0	15.5	8.7	16.7	59.7	0.1	0.0	0.0	---	---	101.7
AHF-S-2-3	3.2	0.7	0.0	15.5	12.7	28.5	42.6	0.4	0.0	0.0	---	---	103.5
AHF-S-2-4	2.3	1.4	14.4	15.6	20.3	33.2	10.5	0.6	0.0	0.0	---	---	98.4
AHF-S-2-5	2.0	12.3	0.0	19.9	26.2	33.0	5.0	0.7	0.0	0.0	Scapolite	1.8	100.8
AHF-S-2-6	10.9	5.1	0.0	19.4	29.9	32.9	0.0	0.5	0.0	0.1	Scapolite	1.4	100.1
AHF-S-2-7	22.0	0.0	0.0	14.3	28.4	35.3	0.0	0.9	0.0	0.0	---	---	101.0
AHF-S-2-8	23.2	0.0	0.0	14.4	27.2	38.4	0.0	1.1	0.0	0.0	---	---	104.4
AHF-S-2-9	25.3	0.0	0.0	14.2	26.2	36.1	0.0	0.9	0.0	0.0	---	---	102.8
AHF-S-2-10	23.5	0.0	0.0	14.7	26.0	37.1	0.0	0.8	0.0	0.0	---	---	102.1
AHF-S-2-11	19.7	0.0	0.0	18.5	24.3	36.2	0.0	1.2	0.0	0.0	---	---	99.9

Appendix B. Mineralogy of Samples from Whole-Rock X-Ray Diffraction Analyses

Sample	Tridymite	Cristobalite	Opal-CT	Quartz	K-spar	Plagioclase	Glass	Hematite	Mica	Hornblende	Other	Other wt%	Total
AHF-M-1-1	0.8	0.0	0.0	10.9	5.8	11.6	68.6	0.4	0.0	0.0	---	---	98.1
AHF-M-1-2	1.1	0.4	9.1	14.6	12.9	23.0	36.5	0.8	0.0	0.0	---	---	98.4
AHF-M-1-3	2.2	4.9	0.0	17.7	19.6	29.6	23.1	0.5	0.0	0.0	Calcite	???	97.6
AHF-M-1-4	2.7	13.0	0.0	16.8	26.5	37.4	0.0	0.7	0.0	0.2	Scapolite	1.9	99.2
AHF-M-1-5	9.4	10.2	0.0	14.4	28.8	32.8	0.0	1.3	0.0	0.2	Scapolite	1.3	98.3
AHF-M-1-6	23.5	0.0	0.0	14.5	27.2	37.3	0.0	1.1	0.0	0.0	---	---	103.5
AHF-M-1-7	21.1	0.0	0.0	15.9	25.5	37.7	0.0	0.8	0.0	0.0	---	---	101.0
AHF-M-1-8	26.2	0.0	0.0	14.0	24.0	36.1	0.0	0.9	0.0	0.0	---	---	101.3
AHF-M-1-9	24.8	0.0	0.0	15.5	24.7	37.5	0.0	0.7	0.0	0.0	---	---	103.2
AHF-M-1-10	24.4	0.0	0.0	13.7	27.4	35.9	0.0	0.7	0.0	0.0	---	---	102.0
AHF-M-2-1	0.5	0.2	0.0	18.7	7.3	14.3	59.5	0.4	0.0	0.0	---	---	101.1
AHF-M-2-2	2.2	10.2	0.0	13.4	22.7	37.2	10.0	0.7	1.1	0.0	Halite	1.2	98.7
AHF-M-2-3	2.2	16.2	0.0	13.9	27.2	36.6	0.0	1.1	0.0	0.1	Scapolite	2.2	99.5
AHF-M-2-4	15.7	2.7	0.0	19.2	25.9	34.7	0.0	0.7	0.0	0.1	Scapolite	1.2	100.3
AHF-M-2-5	19.7	0.5	0.0	17.5	24.9	38.4	0.0	0.7	0.0	0.1	---	---	101.8
AHF-M-2-6	21.9	0.0	0.0	17.5	23.9	35.3	0.0	0.7	0.0	0.0	---	---	99.3
AHF-M-2-7	22.3	0.0	0.0	14.9	24.0	39.8	0.0	0.8	0.0	0.0	---	---	101.7
AHF-M-2-8	22.2	0.0	0.0	12.6	26.4	37.1	0.0	1.1	0.0	0.0	---	---	99.4
AHF-M-2-9	22.0	0.0	0.0	16.9	26.1	36.9	0.0	0.7	0.0	0.0	---	---	102.7
AHF-M-2-10	22.4	0.0	0.0	18.2	25.3	34.3	0.0	1.0	0.0	0.0	---	---	101.2
AHF-M-2-11	15.4	1.5	0.0	17.4	27.1	37.2	0.0	1.0	0.1	0.1	---	---	99.8
AHF-M-2-12	8.0	8.7	0.0	16.3	27.8	37.6	0.0	0.8	0.0	0.0	---	---	99.2

Appendix C. Whole-Rock Geochemistry

Sample Number	SiO_2	TiO_2	Al_2O_3	Fe_2O_3	MnO	MgO	CaO	Na_2O	K_2O	P_2O_5	LOI	Total Maj	Zn	Rb	Sr	Y	Zr	Nb	Ba	Total Trace
AHF-S-1-1	75.25	0.07	11.62	1.49	0.08	0.06	0.43	4.28	4.23	0.00	2.39	97.51	117.5	231.5	14.9	84.1	224.5	116.4	56.4	0.11
AHF-S-1-2	76.44	0.07	11.60	1.44	0.07	0.06	0.32	4.04	4.23	0.01	1.62	98.28	121.6	206.5	15.2	83.4	200.2	95.4	BD	0.09
AHF-S-1-3	76.28	0.07	11.54	1.47	0.07	0.00	0.36	3.60	4.95	0.00	1.54	98.35	105.0	217.0	20.0	88.6	207.7	99.9	52.7	0.10
AHF-S-1-4	77.17	0.08	11.67	1.46	0.08	0.06	0.20	4.10	4.34	0.01	0.71	99.18	119.4	199.3	21.2	83.5	214.0	96.5	115.9	0.11
AHF-S-1-5	75.66	0.07	11.73	1.45	0.07	0.22	0.89	4.14	4.40	0.16	1.08	98.82	94.8	205.4	28.7	73.5	215.5	93.0	BD	0.09
AHF-S-1-6	75.44	0.06	11.23	1.35	0.06	0.16	1.71	4.02	4.24	0.01	1.61	98.29	97.9	195.6	22.2	79.7	190.8	95.3	58.2	0.09
AHF-S-1-7	77.96	0.07	11.44	1.44	0.07	0.00	0.17	4.17	4.30	0.00	0.30	99.61	113.1	204.6	13.2	72.7	198.9	92.7	BD	0.09
AHF-S-1-8	77.87	0.07	11.64	1.37	0.06	0.00	0.35	4.08	4.28	0.00	0.19	99.72	96.7	184.8	19.2	62.1	197.7	74.4	65.6	0.09
AHF-S-1-9	77.28	0.09	11.68	1.51	0.07	0.07	0.38	4.25	4.43	0.00	0.17	99.76	78.9	171.6	22.1	60.1	214.1	68.8	BD	0.08
AHF-S-1-10	77.58	0.09	11.74	1.44	0.06	0.06	0.29	4.13	4.36	0.00	0.16	99.75	81.5	154.5	20.2	55.3	218.0	72.2	78.2	0.09
AHF-S-1-11	77.56	0.09	11.63	1.47	0.06	0.07	0.29	4.09	4.34	0.01	0.32	99.60	73.0	147.0	19.4	47.2	213.7	59.9	BD	0.07
AHF-S-1-12	77.58	0.09	11.70	1.44	0.06	0.06	0.27	4.13	4.36	0.00	0.24	99.68	77.2	138.7	19.1	44.0	208.3	72.5	70.0	0.08
AHF-S-1-13	77.80	0.09	11.60	1.43	0.06	0.00	0.27	4.07	4.34	0.00	0.25	99.67	66.2	139.4	19.5	52.4	198.8	69.8	95.3	0.08
AHF-S-1-14	77.67	0.08	11.75	1.31	0.06	0.00	0.32	4.15	4.42	0.00	0.17	99.76	52.6	144.8	15.6	38.0	202.2	62.4	65.8	0.07
AHF-S-1-15	77.80	0.09	11.55	1.43	0.05	0.06	0.31	3.96	4.36	0.00	0.31	99.62	50.9	140.4	16.0	39.8	200.7	65.3	69.9	0.07
AHF-S-1-16	77.78	0.11	11.66	1.42	0.06	0.08	0.26	3.94	4.32	0.00	0.28	99.63	72.7	105.4	21.8	37.9	212.7	58.7	171.5	0.09
AHF-S-1-17	77.22	0.11	11.91	1.45	0.05	0.08	0.29	4.04	4.39	0.00	0.37	99.55	49.9	107.1	22.8	35.9	229.1	53.2	107.9	0.08
AHF-S-2-1	76.15	0.07	11.74	1.47	0.07	0.00	0.29	4.00	4.23	0.00	1.89	98.02	112.8	221.1	16.0	86.5	214.9	113.2	BD	0.10
AHF-S-2-2	76.29	0.08	11.52	1.49	0.07	0.07	0.52	3.86	4.20	0.00	1.81	98.09	104.4	200.2	22.9	83.6	201.5	100.9	73.5	0.10
AHF-S-2-3	76.51	0.07	11.81	1.54	0.08	0.00	0.39	3.99	4.42	0.00	1.08	98.81	86.9	215.3	21.7	79.8	218.0	108.4	94.8	0.10
AHF-S-2-4	76.27	0.07	12.13	1.49	0.09	0.08	0.32	3.91	4.40	0.07	1.05	98.86	90.7	145.7	19.6	98.4	229.0	106.6	65.8	0.10
AHF-S-2-5	77.55	0.07	11.60	1.44	0.07	0.06	0.18	4.11	4.35	0.02	0.46	99.45	109.4	198.1	14.1	72.5	199.9	95.8	BD	0.09
AHF-S-2-6	77.78	0.07	11.53	1.42	0.07	0.00	0.23	4.17	4.32	0.00	0.31	99.59	168.7	193.5	10.6	92.5	198.6	87.1	52.9	0.10
AHF-S-2-7	77.71	0.07	11.52	1.48	0.07	0.07	0.26	4.15	4.28	0.00	0.30	99.61	92.3	170.8	15.2	80.2	207.7	92.7	61.4	0.09
AHF-S-2-8	77.22	0.09	11.79	1.56	0.07	0.00	0.23	4.25	4.45	0.02	0.24	99.67	91.0	163.8	19.2	90.3	217.4	83.1	65.5	0.09
AHF-S-2-9	77.54	0.10	11.78	1.50	0.06	0.00	0.20	3.99	4.42	0.01	0.34	99.59	74.8	144.7	14.4	57.4	217.1	64.5	BD	0.07
AHF-S-2-10	77.31	0.09	11.92	1.46	0.06	0.00	0.26	4.18	4.47	0.00	0.15	99.75	73.1	140.7	19.8	45.1	213.8	72.1	180.0	0.09
AHF-S-2-11	77.25	0.12	11.66	1.80	0.08	0.15	0.35	3.97	4.26	0.00	0.27	99.64	111.9	120.7	28.3	40.5	194.0	61.8	94.9	0.08
AHF-M-1-1	75.76	0.08	11.69	1.56	0.08	0.00	0.49	3.52	5.04	0.02	1.64	98.25	114.9	243.3	23.2	95.3	241.6	111.2	73.7	0.12
AHF-M-1-2	75.17	0.08	11.64	1.52	0.07	0.16	1.14	3.55	4.66	0.07	1.84	98.05	102.5	190.6	38.1	77.8	206.9	83.8	104.4	0.10
AHF-M-1-3	74.92	0.07	11.70	1.37	0.06	0.13	1.56	3.79	4.28	0.01	2.00	97.91	80.4	155.9	35.7	63.6	198.6	80.4	62.4	0.09
AHF-M-1-4	77.28	0.07	11.85	1.47	0.08	0.00	0.15	4.16	4.39	0.01	0.44	99.46	111.7	207.6	15.6	63.0	210.8	105.8	90.7	0.10
AHF-M-1-5	76.64	0.08	12.08	1.61	0.08	0.00	0.27	4.29	4.46	0.00	0.40	99.50	112.5	219.4	14.1	93.2	234.3	115.3	BD	0.10
AHF-M-1-6	76.81	0.09	11.89	1.61	0.07	0.08	0.24	4.15	4.37	0.01	0.60	99.31	98.9	168.2	17.1	54.9	226.8	72.6	48.4	0.09

Appendix C. Whole-Rock Geochemistry

Sample Number	SiO_2	TiO_2	Al_2O_3	Fe_2O_3	MnO	MgO	CaO	Na_2O	K_2O	P_2O_5	LOI	Total Maj	Zn	Rb	Sr	Y	Zr	Nb	Ba	Total Trace
AHF-M-1-7	77.38	0.08	11.75	1.44	0.06	0.06	0.28	4.14	4.40	0.00	0.33	99.59	79.3	154.1	20.4	48.5	193.2	67.7	53.0	0.08
AHF-M-1-8	77.60	0.09	11.55	1.47	0.06	0.06	0.28	4.10	4.35	0.00	0.37	99.56	76.1	143.7	19.8	40.2	210.2	81.2	BD	0.07
AHF-M-1-9	77.10	0.10	11.73	1.65	0.06	0.06	0.30	4.15	4.34	0.00	0.43	99.49	92.4	152.9	22.1	45.2	217.7	70.5	BD	0.08
AHF-M-1-10	77.23	0.09	11.92	1.42	0.05	0.00	0.32	4.18	4.50	0.00	0.22	99.70	77.5	140.6	13.8	34.7	212.4	72.8	57.3	0.08
AHF-M-2-1	76.31	0.07	11.80	1.51	0.07	0.00	0.26	3.53	4.99	0.01	1.35	98.55	84.6	204.3	11.3	97.3	221.2	100.7	BD	0.09
AHF-M-2-2	73.51	0.07	11.03	1.27	0.06	0.06	0.34	6.28	4.14	0.00	3.15	96.76	78.1	178.8	18.3	67.3	177.0	78.6	BD	0.08
AHF-M-2-3	77.28	0.07	11.67	1.42	0.06	0.00	0.32	4.23	4.38	0.00	0.46	99.45	93.5	203.0	11.7	88.6	210.5	91.8	BD	0.09
AHF-M-2-4	77.85	0.07	11.48	1.44	0.07	0.00	0.19	4.15	4.31	0.00	0.34	99.56	86.3	193.1	12.4	56.5	198.4	104.5	74.0	0.09
AHF-M-2-5	77.64	0.08	11.69	1.45	0.07	0.00	0.21	4.21	4.39	0.00	0.18	99.74	97.4	171.2	11.6	70.2	195.3	76.3	BD	0.08
AHF-M-2-6	78.12	0.08	11.35	1.41	0.06	0.06	0.28	4.04	4.29	0.00	0.23	99.70	72.4	140.7	19.6	61.9	193.9	58.5	BD	0.07
AHF-M-2-7	77.62	0.09	11.84	1.45	0.06	0.06	0.28	4.02	4.35	0.00	0.15	99.77	68.7	135.1	16.0	37.9	206.0	78.1	53.0	0.08
AHF-M-2-8	77.69	0.08	11.81	1.40	0.05	0.00	0.23	3.99	4.43	0.00	0.25	99.67	69.3	139.4	14.1	35.0	198.1	66.5	99.6	0.08
AHF-M-2-9	77.59	0.09	11.79	1.41	0.05	0.00	0.21	4.02	4.46	0.00	0.30	99.63	61.9	132.7	12.4	43.8	205.6	65.7	61.5	0.07
AHF-M-2-10	77.58	0.10	11.65	1.48	0.06	0.08	0.26	3.90	4.26	0.00	0.56	99.37	76.6	126.1	17.4	39.3	196.1	62.5	BD	0.07
AHF-M-2-11	77.74	0.11	11.58	1.49	0.06	0.08	0.32	4.00	4.34	0.00	0.20	99.72	69.4	117.5	26.2	30.7	211.5	54.1	163.0	0.08
AHF-M-2-12	77.13	0.12	11.69	1.52	0.05	0.09	0.44	3.97	4.33	0.00	0.57	99.34	70.0	115.5	38.3	28.2	230.6	56.9	171.2	0.09

*Trace totals as oxides. Analytical uncertainties are 2 sigma, in same units as analyses. Units are in weight % (normalized to 100%) for major oxides and ppm for trace elements. Analytical uncertainties are available upon request from the authors. V, Cr, and Ni concentrations are below detection limits and therefore not reported.
BD = below detection limits, LOI = loss on ignition.